105學年度

學生專題研究論文集

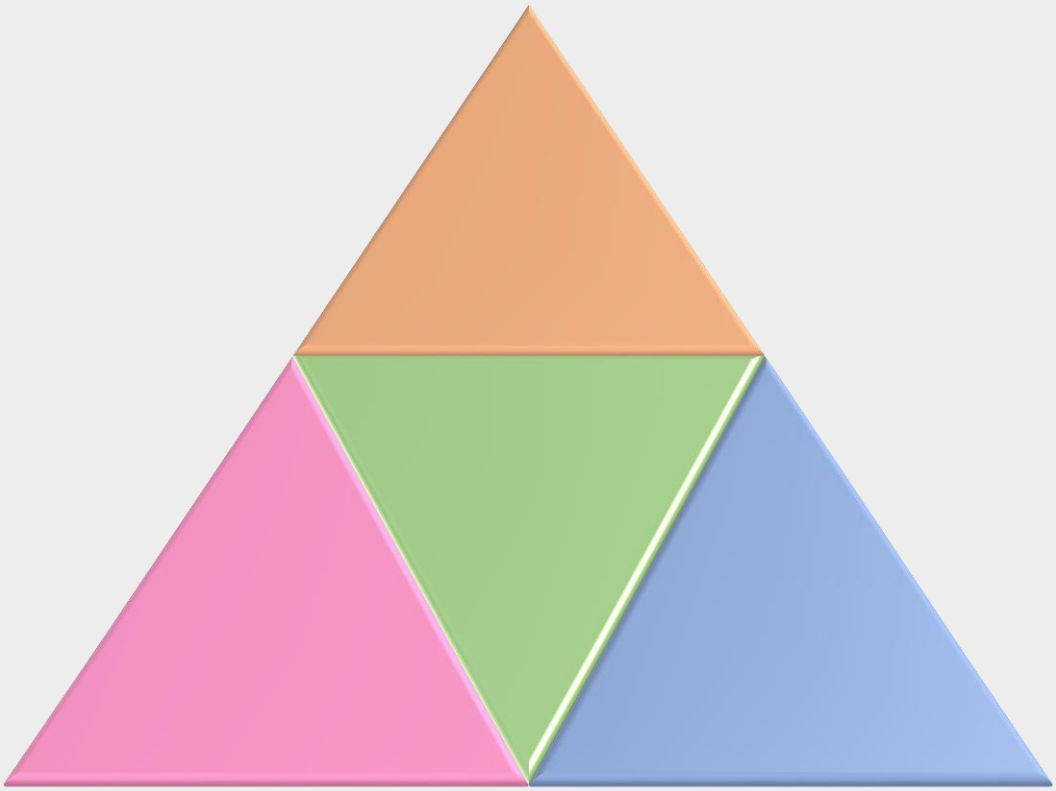

東海大學應用物理系

目錄

Structure and magnetic properties of 300-nm-thick FePt films with Hf underlayer

C.Y. Shen[a], Y.W. Wang[b], H.W. Chang[b]*, C.R. Wang[b]
[a] Department of Electrical Engineering, Hsiuping University of Science and Technology, Taichung 412, Taiwan
[b] Department of Applied Physics, Tunghai University, Taichung 407, Taiwan

Introduction

- In the past decades, $L1_0$ FePt is one of the permanent magnetic materials that have received considerable attention. Outstanding hard magnetic properties in thin film form.
- In permanent magnetic applications, the performance of a magnetise valuated by energy product $(BH)_{max}$, which denotes the stored energy density.
- In the case of FePt, adding appropriate B and Co contents into FePt alloys was helpful in developing the isotropic.
- Multilayer, deposition Exchange coupled FePt/Fe bilayer films and FePt-Fe_3Pt nanocomposite films were reported to improve $(BH)_{max}$. Grain refining by annealing control, strain/stress engineering, underlayering, anddoping were also found to significantly increase $(BH)_{max}$ of FePt films.

Experiment

XRD
EDS
TEM
MFM
VSM

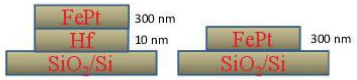

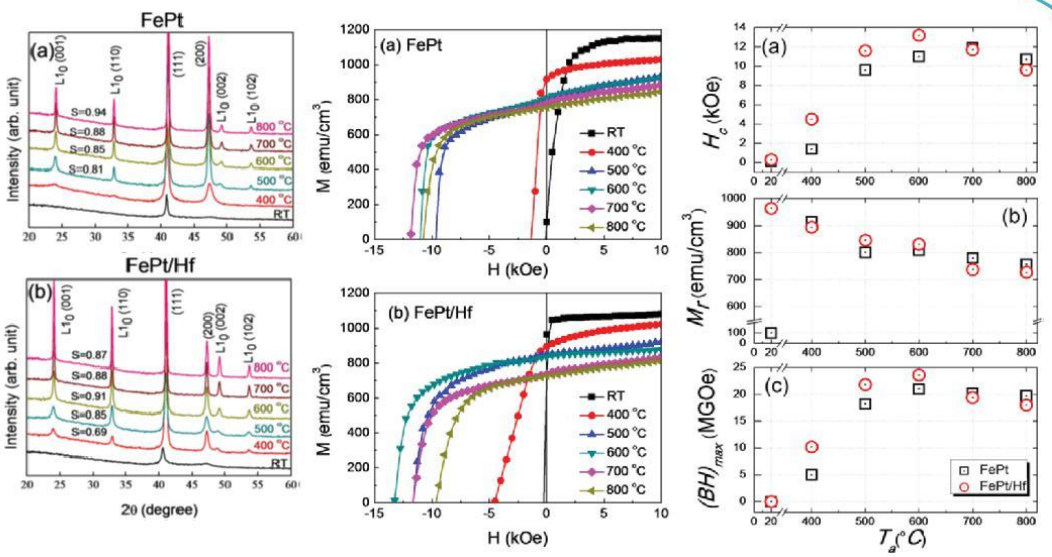

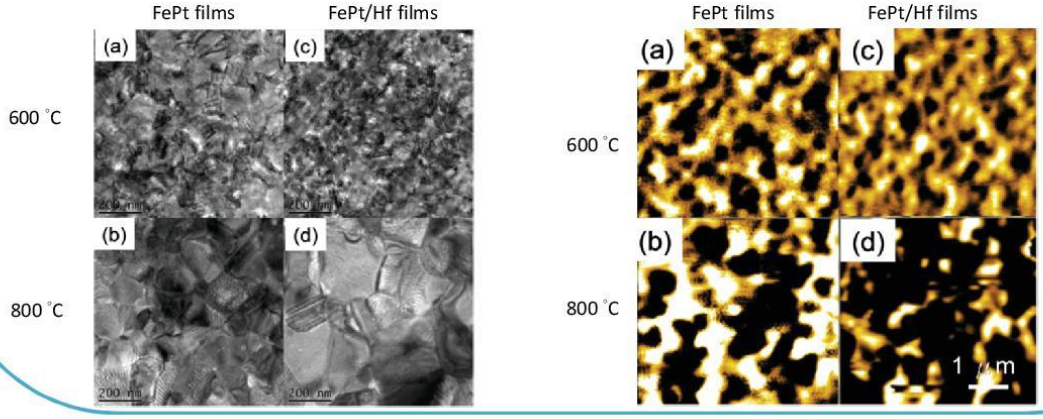

Conclusons

- At as-deposited state, two series of films were disordered exhibiting similar saturation magnetization and low Hc below 0.3 kOe.
- $(BH)_{max}$ of FePt films was greatly enhanced from 5.0–21.0 MGOe for single layer to 10.2–23.6 MGOe for Hf-underlayered films annealed in Ta range of 400–600 °C, respectively.
- Nevertheless, the severe interdiffusion between the Hf and FePt layers at higher Ta = 800 °C resulted in the decreased S, coarsened surface morphology, grain and magnetic domain sizes, causing decreased $(BH)_{max}$.

Effect of swelling of a photoresist on electromagnetic resonance of terahertz metamaterials

Chia-Yi Huang* and Chia-Chun Chen(江偉凡)
Department of Applied Physics, Tunghai University, Taichung 407, Taiwan
*Author for Correspondence: chiayihuang@thu.edu.tw

Abstract

This work uses isopropyl alcohol (IPA) to develop a photoresist. IPA dissolves the photoresist that is not exposed to UV light. The swelling of the photoresist distorts the split-ring resonators (SRRs). The distorted SRRs have a larger loop length, smaller line width, and smaller split gap than undistorted SRRs. The change in the dimensions of the SRRs is caused by the extension of the SRR arms in their longitudinal directions. The resonance frequency of the distorted SRRs is smaller than that of the undistorted SRRs, and the resonance frequency decreases with the development time. The resonance frequency of the distorted SRRs depends on not only their dimensions, but also the bending of their arms. The distorted SRRs in this work have a frequency tuning range with a maximum width of 0.13 THz. The method that is proposed herein uses IPA to fabricate passively tunable terahertz metamaterials, which exhibit the advantages of high reliability, low cost, and ease of fabrication.

Sample Fabrication

Figure 1 presents the process for fabricating test samples. Identical polyester (PET) substrates with a thickness of 175 μm are used. A 200 nm-thick silver film and a 5 μm-thick PR layer (ENPI202, Everlight Chemical Industrial Co.) are sequentially deposited on each PET substrate. A split-ring resonator (SRR) array on a photomask is transferred onto the PR layers under UV irradiation. After the PR layers have been irradiated with UV, they are baked at 100˚C. The baked PR layers are then developed using isopropyl alcohol (IPA) rather than the specific developer of the PR. This development process sets this work apart from previous studies of metamaterials . The test samples have different development times: 45, 90, and 135 min. After they are developed, the test samples are immersed into a metal etchant (F-CHEM Enterprise Co.) to etch the silver layers. The etching time of each sample is approximately 1 s.

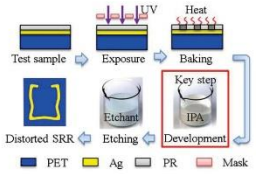

Fig. 1. (a) Fabrication of test samples.

Experimental Results (I)

Figure 3 presents the terahertz spectra of the reference sample, test samples that underwent PEB at 100˚C and were developed for 45, 90, and 135 min, and a test sample that underwent PEB at 95˚C and was developed for 45 min. These spectra are obtained using a commercial terahertz spectrometer(TPS 3000, TeraView), and the polarization of normally incident terahertz waves is set parallel to the x axis, as presented in Fig. 1(b). The resonance peak of the reference sample is at 0.65 THz, and the resonance peak of the test sample that underwent PEB at 100˚C and was developed for 45 (90) min is at 0.63 (0.57) THz. This result depicts that the resonance peak of the test sample that was developed for 45 (90) min is redshifted by 0.02 (0.08) THz. The redshifts of the spectra of the test samples arise from the increase in the loop length of the SRRs , the decrease in their line width , and the decrease in their split gap. This result reveals that a test sample reaches its minimum resonance frequency as it is developed for a particular development time. Therefore, a development time of 90 min yields a larger frequency tuning range than development times of 45 and 135 min at a PEB temperature of 100˚C. The resonance frequency (0.52 THz) of the test sample that underwent PEB at 95˚C is redshifted from that (0.65 THz) of the reference sample, as displayed in Fig. 3. Therefore, this test sample has a frequency tuning range with a maximum width of 0.13 THz herein. The distorted SRRs can be used to develop passively tunable terahertz devices such as filters, absorbers, sensors, and spectral imagers.

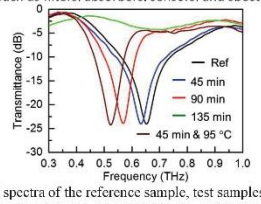

Fig. 3. Experimental spectra of the reference sample, test samples that underwent PEB at 100˚C and were developed for 45, 90, and 135 min, and test sample that underwent PEB at 95˚C and was developed for 45 min.

Experimental SEM

Figures 2(f)–2(h) display the scanning electron microscope (SEM) images of the reference sample, the test sample that was developed for 45 min, and the test sample that was developed for 90 min, respectively. The results in Figs. 2(f)–2(h) reveal that IPA can be used to distort the SRRs in the test samples. The distortion of the SRRs is caused by the swelling of the PR in IPA. A relatively low post-exposure baking (PEB) temperature of 95˚C is applied to a test sample to increase the distortion of SRRs. the PR layer that underwent PEB at 95˚C and was developed for 45 min is softer than the PR layer that underwent PEB at 100˚C and was developed for 90 min.

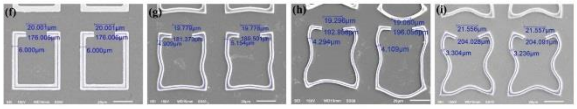

Fig. 2. SEM images of (f) reference sample, test samples that underwent PEB at 100˚C and were developed for (g) 45 and (h) 90 min, and (i) the test sample that underwent PEB at 95˚C and was developed for 45 min.

Experimental Results (II)

A simulation is performed using computer simulation technology (CST) software to verify the dependence of the resonance spectra on the dimensions of the distorted SRRs.
As the arms of the distorted SRRs are bent, the consequent shift of the resonance spectrum is caused not only by the asymmetric electrical coupling but also by the change in the areas that are enclosed by the distorted SRRs. The electromagnetic resonance of an SRR can be treated as a simple inductance capacitance resonance. The resonance frequency (f) of the SRR is given by the equation $f = 1/2\pi\sqrt{LC}$, where C is the capacitance of the split gap of the SRR, and L is the inductance of the loop of the SRR and is directly proportional to the area that is enclosed by it. The equation reveals that the outward (inward) bending of the arms of an SRR increases (reduces) the enclosed area, increasing (reducing) its inductance, resulting in a redshift (blueshift) of its resonance spectrum. Accordingly, both the asymmetric electrical coupling and the change in the enclosed area shift the resonance spectrum of the distorted SRRs as their arms bend.

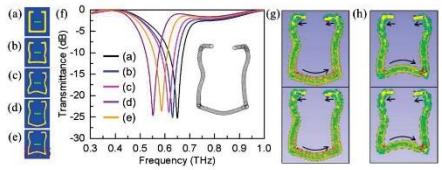

Fig. 4. Simulated units of (a) the reference sample and (b) the test sample that underwent PEB at 100˚C and was developed for 45 min. (c) and (d) Simulated units of the test sample that underwent PEB at 100˚C and was developed for 90 min. (e) Simulated unit with the same dimensions as that in (d) but with its bottom arm (inside a red dashed frame) bent inward toward the geometrical center of the simulated unit. (f) Simulated spectra of SRR arrays, each of which comprises one of five simulated units. The inset presents a simulated unit constructed from small circular disks. (g) Current flow distribution of the SRR array that comprises the SRR unit in (d). (h) Current flow distribution of the SRR array that comprises the SRR unit in (e).

Conclusion

- the distorted SRRs are fabricated by the swelling of a PR in IPA during its development.
- The resonance spectrum of the distorted SRRs is redshifted from that of undistorted SRRs, and the spectral redshift increases with the development time.
- The simulated results reveal that the resonance frequency of the distorted SRRs depends not only on their dimensions, but also the bending of their arms.
- The distorted SRRs in this work have a frequency tuning range with a maximum width of 0.13 THz. Therefore, the distorted SRRs can be used to develop passively tunable terahertz metamaterials.

Acknowledgement

The authors would like to thank the Ministry of Science and Technology of Taiwan for financially supporting this research under Contract No. MOST 104-2112-M-029 -004 -MY3.

References

[1] P. Pitchappa, C. P. Ho, L. Dhakar, and C. Lee, Optica 2, 571 (2015).
[2] B. Wu, B. Li, T. Su, and C. H. Liang, PIERS Online 2, 710 (2006).

Observation of charge coupling in InGaP/InGaAs/Ge triple-junction solar cells by electric modulus spectroscopy

Chun-Ying Huang, Gia-Wei Shu, Kuan-Yu Lai, Bi-Cheng Lei, and Forest Shih-Sen Chien
Department of Applied Physics, Tunghai University, Taichung 40704, Taiwan

Abstract

電荷耦合效應的觀察對於三接面太陽能電池（TJSC）的電子移動行為是非常重要的。電模量(M)頻譜搭配適當的雷射被證明是研究InGaP / InGaAs / Ge TJSC中各個子電池的內部電特性的有效方法。利用分別對應的雷射激發三個單獨的子電池，對應到M的虛部中的不同的特徵峰，觀察被激發的子電池與子電池之間的電荷耦合，這種方法提供了TJSC設計的電荷耦合信息。

Motivation

- 多接面太陽能電池已經廣泛應用，轉換效率高達40%， TJSCs具有高效率的前途。
- 子電池與子電池之間的不匹配仍然存在且限制了他們的進一步發展，因為一個子電池具有較低光電流，會限制整個太陽能電池的電流產生。
- III-V TJSC是由三個或三個以上子電池組成的複雜設備，電荷僅能透過子電池間的接面通過，因此建立這種非破壞性診斷電池內部接面電荷耦合特性的技術十分重要。

Results and Discussion

元件結構

- 532 nm, 808 nm , 1064 nm雷射分別對應到InGaP, InGaAs, Ge

比較M平面與Z平面差異

Complex impedance spectra (Z' vs. Z")

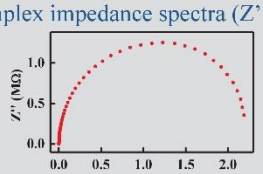

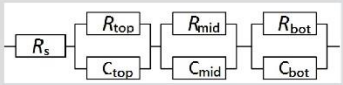

TJSC等效電路圖

- 半圓直徑對應到電阻R
- Bode plots虛部(Z" vs. frequency)
  產生的峰值對應到特徵頻率$f_c=1/(2\pi RC)$

Complex electric modulus M

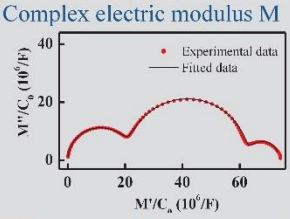

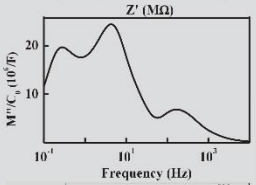

- $M=i\omega C_0 Z$
- 半圓直徑對應到1/C
- M "的Bode plot 也會產生一個波峰對應到特徵頻率f_c =1/2 C

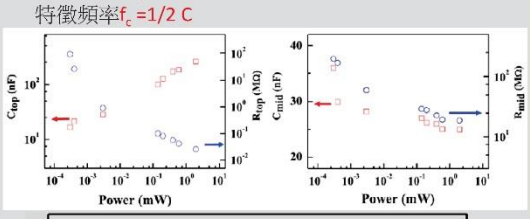

TJSC at zero bias under various 532 nm illumination power

Junction Capacitance

$$C' = \left\{ \frac{e\epsilon_s N_a N_d}{2(V_{bi} + V_R)(N_a + N_d)} \right\}^{1/2}$$

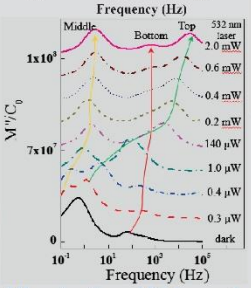

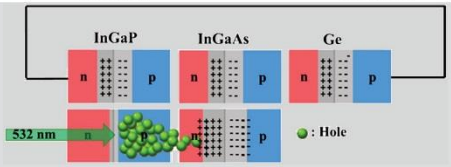

- 532nm雷射top cell吸收產生順偏效果會造成空乏區變小，空乏區變小對應到的電容就是變大，因為打了很多載子進去，載子變多的時候，會造成這個電阻變小，載子擴散至middle cell產生逆偏。

Illumination 1064 nm laser with fixed 532 nm and 808nm laser

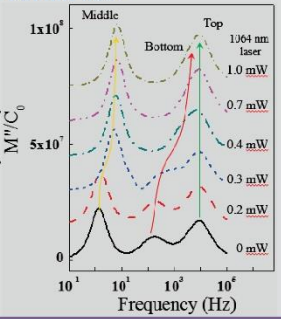

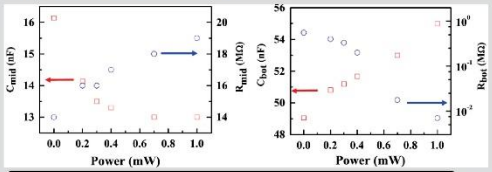

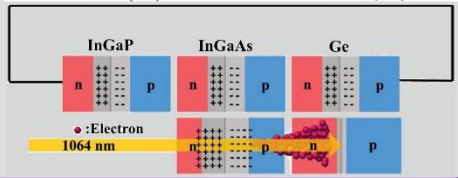

- 1064nm雷射bottom cell吸收產生順偏效果會造成空乏區變小，空乏區變小對應到的電容就是變大，因為打了很多載子進去，載子變多的時候，會造成這個電阻變小，載子擴散至middle cell產生逆偏。

Conclusion

- 能藉由選擇不同雷射波長激發不同位置junction來達到觀察不同junction間相互的影響
- 我們可以藉由這種方法觀察太陽能電池內部載子流動與charge coupling的現象
- 這種方法不會破壞太陽能電池結構

references

Appl. Phys. Lett. **110**, 033901 (2017); doi: 10.1063/1.4974308

Acknowledge

Ministry of Science and Technology of Taiwan under the Contract No. MOST 105-2112-M-029-001-MY3.

Application of Carbon Paste as Counter Electrodes in Dye-Sensitized Solar Cells

G. -Y. Lin[1] , B. -C. Lei[1], C. -E. Cheng[1,2] , F. S.-S. Chien[1]
[1]Department of Applied Physics, Tunghai University, Taiwan
[2]Department of Photonics, National Chiao Tung University, Taiwan

Abstract

自1991年M. Grätzel的團隊改善了染料敏化太陽能電池(dye-sensitized solar cells，DSCs) 後，一般的DSCs皆以白金(Pt)作為對電極。但因其過於昂貴的價格，本研究希冀藉碳膠來取代Pt作為DSCs的對電極。實驗中分別使用30%的酒精溶劑碳膠、100%的酒精溶劑碳膠、30%的水溶劑碳膠、100%的水溶劑碳膠及一個Pt對照組。由光伏特性*J*-V曲線測量結果發現，使用水溶劑碳膠為對電極的DSCs其表現相對於使用酒精溶劑碳膠為對電極的DSCs佳，整體表現也與使用Pt為對電極的太陽能電池較為接近。總體表現則以100%的水溶劑碳膠最好(J_{sc}：5.57 mA/cm^2；V_{oc}：0.56V)，太陽能電池能量轉換效率也以其1.33%為最佳。

Motivation

Pt擁有優異的催化能力，因此傳統染料敏化太陽能電池對電極(counter electrode)皆由Pt所組成。但是Pt為目前最昂貴的金屬之一，若要達成普及大面積製作將會提高製作成本。目前有相當多的碳材料適合被應用於太陽能電池上，但本研究仍想以更加簡單的方法來取代Pt。因此碳膠即為首選，它取得管道眾多且價格相對便宜，若能將效率做到與Pt相近，將是一個良好的取代材料。

Results and Discussion

Device Fabrication

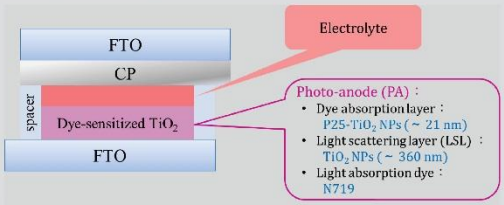

Counter Electrode

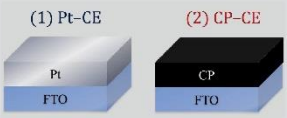

- 鍍 5nm Pt 於 FTO 基板上(Sputter)
- 碳膠用刷子均勻塗抹於FTO基板上
- 碳膠塗抹前先以Plasma Cleaner改變玻璃的親水親油性

Photovoltaic Performance of DSCs

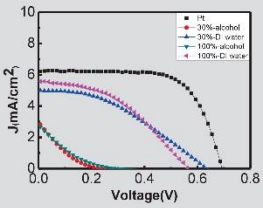

DSCs	Eff. (%)	J_{sc} (mA/cm^2)	V_{oc} (mV)	FF (%)
Pt	2.95	6.21	686	69.32
30% alcohol	0.11	2.83	238	16.26
30% DI water	1.23	5.00	624	39.28
100% alcohol	0.12	2.69	284	16.30
100% DI water	1.33	5.57	562	42.49

- 以碳膠為對電極的DSCs不管是短路電流、開路電壓、填充因子與轉換效率皆較以Pt為對電極的DSCs低
- DI水溶劑的碳膠整體的表現都比酒精溶劑的碳膠要好

DSCs	R_s (Ω)	R_{ct} (Ω)	CPE 1-T (μF)	CPE 1-P	f_{ct} (Hz)	R_{rec} (Ω)	CPE 2-T (μF)	CPE 2-P	f_{rec} (Hz)
Pt	5.58	8.73	31.45	0.91	1244.56	129.10	867.62	0.94	1.64
30% alcohol	6.94	989.70	37.05	0.90	6.36	13725	19.33	0.89	0.71
30% DI 水	8.31	18.71	433.63	0.54	1110.63	544.90	567.40	0.80	0.69
100% alcohol	7.26	1436	30.18	0.89	5.36	9945	26.63	0.89	0.71
100% DI 水	7.12	166.50	158.65	0.29	15.91	338.40	528.53	0.84	1.25

Impedance Performance of DSCs

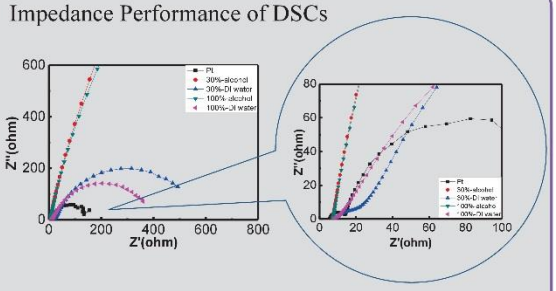

- 以水溶劑碳膠為對電極的DSCs其電催化效應較使用酒精溶劑碳膠為對電極的DSCs佳
- 以水溶劑碳膠為對電極的DSCs其電子轉移能力較使用酒精溶劑碳膠為對電極的DSCs佳(fct較佳)
- 以水溶劑碳膠為對電極的DSCs相比於使用酒精溶劑碳膠為對電極的DSCs 其電子電洞對再結合能力差異不大
- 未來本研究將著重於改善碳膠本身的特性，加入少許的奈米碳管，將塗抹完碳膠的對電極拿去鍛燒、照紫外線或打電漿，去除掉空氣中汙染碳膠的粒子

Conclusion

雖然目前已進行過的實驗結果，離本研究所期望的目標尚有一段差距，但是從實驗中可以發現以水溶劑碳膠為對電極的DSCs其電子轉移能力相對於使用酒精溶劑碳膠為對電極的DSCs要優秀，漏電途徑亦減少許多。總體表現則以100%的水溶劑碳膠最好(J_{sc}：5.57 mA/cm^2；V_{oc}：0.56V)，太陽能電池能量轉換效率也以其1.33%為最佳。

Acknowledge

Tunghai University and the Ministry of Science and Technology, Taiwan, under Grant No. NSC 102-2112-M-029-005-MY3.

Structure and Ferroelectric Properties of Sm-doped $BiFeO_3$ Polycrystalline Films

C. F. Chang (張家逢), Ting-Kai Lin(林庭楷), H.W. Chang(張晃暐)[1*], C.R. Wang(王昌仁)[1]

Department of Applied Physics, Tunghai University, Taiwan

I. INTRODUCTION

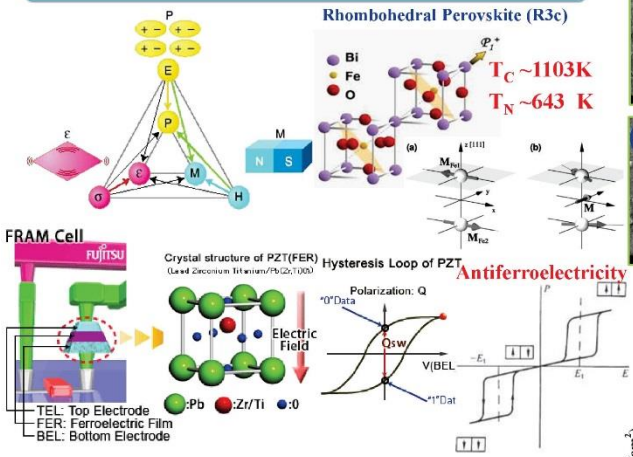

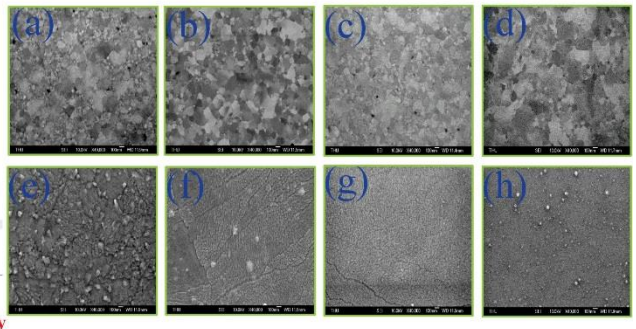

FIG. 2. SEM images of Pt20 nm layer (a) x = 0.05 (b) x = 0.10 ,(c) x = 0.14 ,(d) x = 0.1 6on the glass substrates prepared by pulsed laser deposition at 450 °C: $Bi_{1-x}Sm_xFeO_3$ (a) x = 0.05 (b) x = 0.10 ,(c) x = 0.14 ,(d) x = 0.16 on Pt 20 nm on the glass substrates prepared by pulsed laser deposition at 450 °C

II. EXPERIMENT

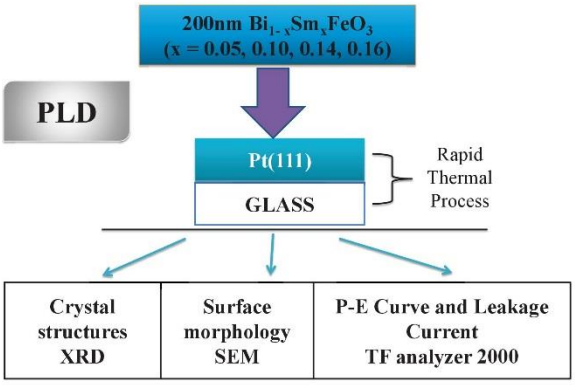

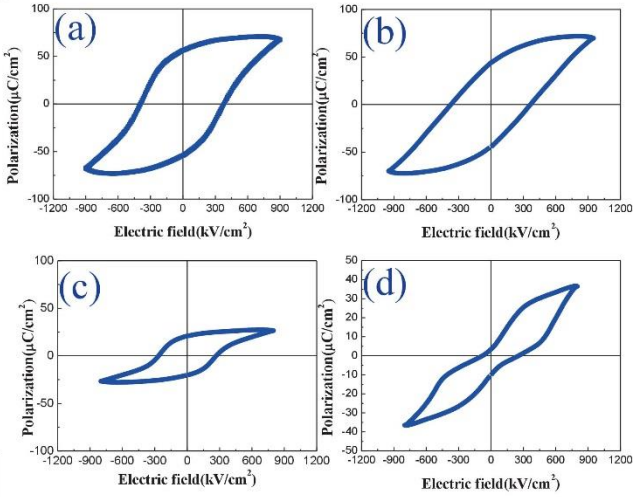

FIG. 4 . P-E curves of (a) x = 0.05. (b) x = 0.10. (c) x = 0.14. (d) x = 0.16 on Pt 20 nm on the glass substrates prepared by pulsed laser deposition at 450 °C

III.RESULT AND DISCUSSION

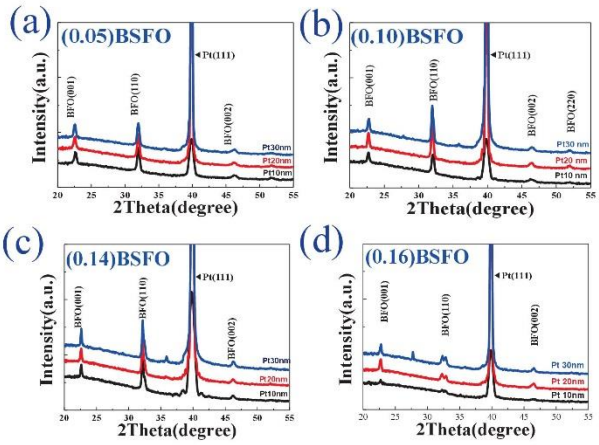

FIG. 1. XRD images of $Bi_{1-x}Sm_xFeO_3$ (a) x = 0.05 (b) x = 0.10 ,(c) x = 0.14 ,(d) x = 0.16. at 450 °C on various Pt thickness on the glass substrates.

IV . CONCLUSIONS

- XRD structural analysis shows that a pure perovskite phase is present for all BSFO films prepared by pulsed laser deposition: rhombohedral structure for BFO with x = 0.05-0.14, but orthogonal structure appear to coexist with rhombohedral for higher x =0.16.
- Due to a smaller ionic radius for Sm^{3+} (0.964 Å) than Bi^{3+} (1.03 Å), Sm substitution for Bi shrinks the BSFO lattice.
- SEM analysis shows that all Pt bottom electrodes exhibit flat surface with large Pt(111) grain, on the other hand, the size of BFO grain is reduced with increasing Sm content.
- The studied BSFO films prepared by pulsed laser deposition at 450 °C shows a good ferroelectric properties, and polarization and coercive field induces reduced with increasing the Sm concentration.
- For higher Sm content, BSFO thin films showed antiferroelectric behavior due to the appearance of orthogonal structure.
- The experiment will still continue be studied.

Influences of sintering temperature on low-cost carbon paste based counter electrodes for dye-sensitized solar cells

Chun-Ying Huang[1], Guan-You Lin[1], Pei-Te Lin[1], Jhih-Wei Chen[2], Chia-Hao Chen[2], and Forest Shih-Sen Chien[1,*]
[1]Department of Applied Physics, Tunghai University, Taiwan
[2]National Synchrotron Radiation Research Center, Taiwan

Abstract

自1991年M. Grätzel的團隊改善了染料敏化太陽能電池(dye-sensitized solar cells，DSCs)後，一般的DSCs皆以白金(Pt)作為對電極。但因其過於昂貴的價格，本研究希冀藉低成本碳膠(CP)並改變不同溫度燒結後來取代Pt作為DSCs的對電極。實驗中使用無、200℃、250℃、300℃燒結碳膠，並證明了通過在300℃燒結下，電池整體轉換效率4.9%，與白金的對電極5.7%相當，燒結後的CP結晶質量提高，降低電池串聯電阻，同時CP表面積的增加，三碘化物的還原率增加。

Motivation

1. 利用低成本碳膠(CP)取代價格昂貴的白金(Pt)，作為對電極。2. 簡單大面積製作。3. 探討碳膠處理後所產生變化。4. 改變碳膠的處理，而去探討對於電池的影響。

Results and Discussion

Device Fabrication

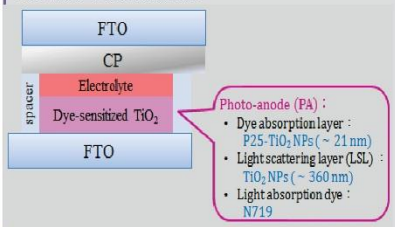

Photovoltaic Performance of DSCs

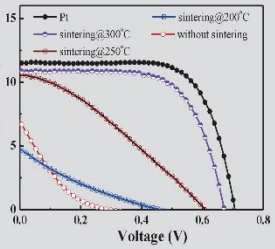

CE	Sintering temp. (°C)	Eff. (%)	Jsc (mA/cm²)	Voc (mV)	FF (%)	Sheet resistance (Ω/□)
Pt	-	5.74	11.50	701	71.07	7.92
CP	-	0.31	6.92	284	15.89	3.5×10^4
CP	200	0.42	4.66	454	19.12	9.0×10^3
CP	250	2.06	10.52	609	32.02	1.8×10^3
CP	300	4.88	10.85	670	67.18	1.6×10^3

Impedance Performance of DSCs

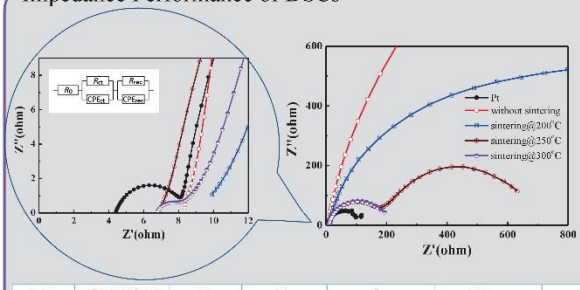

XRD patterns、SEM

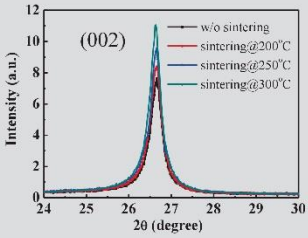

CE	Sintering temp. (°C)	R_0 (Ω)	R_{ct} (Ω)	f_{ct} (Hz)	R_{rec} (Ω)	f_{rec} (Hz)
Pt	-	4.43	3.83	3038	102	1.14
CP	-	11.44	2288	6.69	372	0.77
CP	200	10.06	607	26.2	2004	1.01
CP	250	7.11	171.6	139	524	0.67
CP	300	7.02	1.54	1526	206	0.86

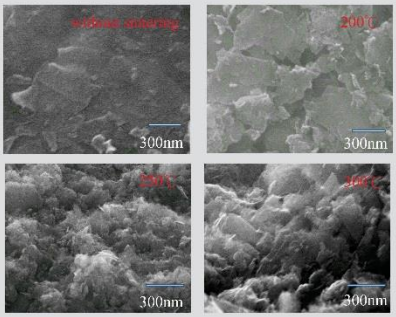

- 隨著溫度提升，能得到較高的Jsc、FF、Eff。
- R_0為串聯電阻，溫度改變，R_0明顯降低，呼應四點探針的電阻率量測。
- 將溫度提高至300℃時，CP的R_{ct}電子轉移能力與Pt相當。
- FF的增強主要為電池內部電阻降低，其來源為R_0及Rct的改善。
- 隨著溫度改變，(002)峰值強度增強，CP質量提高。
- 燒結過程能夠使表面積增加，利於電子轉移能力。

Conclusion

1. 基於CP的CE的DSSC的光伏性能隨著燒結溫度的上升而提高。2. 透過XRD的幫助下，在300℃下燒結提高了CP膜的結晶質量，因此CE內部的載子更有效的傳輸。3. 此外SEM的結果說明，燒結後CP的粗糙度明顯提升，表面積增加，有利於電極和電解液的還原性能。4. 以碳膠比較，整體表現來說燒結300 ℃ 的Jsc、FF、Eff較為出色，並接近白金表現，對於處理過後的CP來說，是一種有潛力適合當作白金的替代品。

References

1. B. O'Regan and M. Grätzel, Natrue **353, 737** (1991)
2. C. Y. Huang, P. H. Chen, Y. J. Wu, H. P. Chiang, J. S. Hwang, P. T. Lin, K. Y. Lai, F. S. S. Chien and T. Y. Lin, Japanese J. Appl. Phys. **56**, 045201 (2017).
3. C. E. Cheng, Y. C. Lin, S. Y. Tsai, Z. K. Lin, P. C. Lee, H. Y. Miao, C. S. Chang and F. S. S. Chien, J. Phys. D: Appl. Phys, **48**, 355107 (2015).

目前向Japanese J. Appl. Phys 投稿中。

Terahertz Waveguide Using Rolled Liquid Crystal Polymer Films

Yu-Yu Chen (陳瑜瑜) , Chia-Yi Huang (黃家逸)

Department of applied physics, Tunghai University, Taichung, Taiwan

Abstract

A liquid crystal polymer (LCP) film comprises a nematic LC (HTW114200-100, Fusol Material), monomer (RM-257, Sigma-Aldrich) and photoinitiator (IRG-184, Sigma-Aldrich). The LCP film is rolled into a hollow cylinder. The hollow cylinder is put in a terahertz spectrometer. Experimental results reveal that the hollow cylinder can confine and guide terahertz waves. As a result, the rolled LCP film can be used to develop terahertz waveguides.

Introduction

Using polymer-stabilized liquid crystal, since the network structure formed by the polymer liquid crystal can stabilize the nematic liquid crystal, in the high concentration polymer-stabilized the nematic liquid crystal can be polymerized into a thin film. This polymer film have capability to align the LC molecules and can polarized light because of the birefringence of LC molecules. By adding additional electric field, LC molecules will change its align direction so that light penetrates or can not penetrate. Under the terahertz wave, we expect that the change of the liquid crystal direction can be taken as the terahertz guide wave . It is possible to absorb or directly penetrate the terahertz wave because of the liquid crystal axis when the voltage is not applied or be applied. Roll the film into a hollow cylinder for the liquid crystal array in long strings, making terahertz waves irradiated to the film will feel the liquid crystal is a thickness rather than just a liquid crystal molecules.

Fabrication

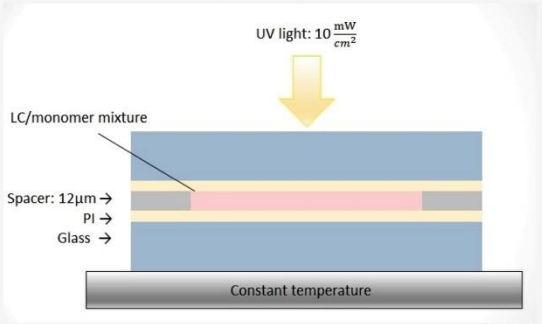

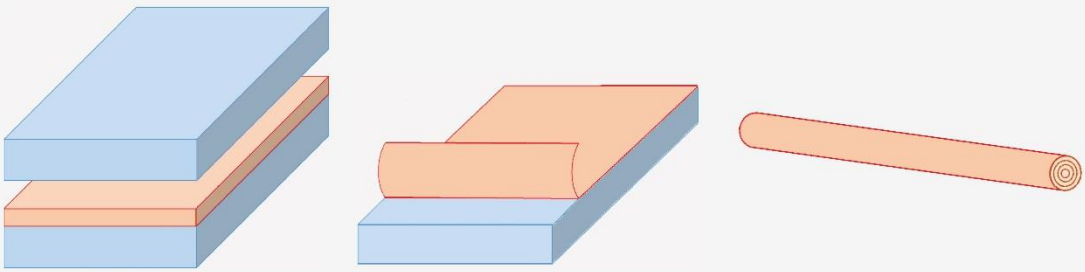

Acknowledgments

The authors would like to thank the Ministry of Science and Technology of Taiwan for financially supporting this research under Contract No. MOST 104-2112-M-029 -004 -MY3.

The Investigation of Polyethylene Terephthalate Substrate with Different Incident Angle of Terahertz Beam

Chun-Chien Huang (黃鈞阡), Chee-Chao Lee (李志超) and Chia-Yi Huang* (黃家逸)
*chiayihuang@thu.edu.tw
Department of Applied Physics, TUNGHAI UNIVERSITY, Taichung, Taiwan.

Abstract

Polyethylene terephthalate (PET) is commonly used to act as the substrates of plasmonic structures because its transmittance is high at the terahertz regime. In this study, terahertz waves are incident to a PET substrate with an area of 2 cm × 2 cm. The normal axis of the substrate is set to be perpendicular to the propagation direction of the waves, and makes an angle of θ with respect to the electric field of the waves.

As θ = 16° (-14°), the PET substrate has a transmission dip at 0.6423 THz (0.7271 THz), and the transmittance at the dip is –95.18 dB (-84.08 dB), as presented in Fig. 2. Such transmittances are lower than the resonance transmittances of terahertz metamaterials. This result cannot be found in polycarbonates and polydimethylsiloxane substrates. As a result, the PET substrate is a high-performance band-stop filter at the terahertz regime.

Experiment

Cut the Polyethylene terephthalate (PET) substrate in to two different sizes, which is 2 cm × 2 cm and 2 cm × 3 cm, then flatten it by heating at 80 degree Celsius for 20 minutes, and let it down to room temperature. Place PET substrate on THORLABS High-Precision Rotation Mount which combined in TeraView TPS Spectra 3000, the terahertz transmission spectrum is measured.

During the experiment, the substrate is set to perpendicular the propagation direction of the waves, the angle between propagation direction of the waves and PET substrate is defined as θ. When PET substrate's long side is parallel with propagation direction of the waves, θ = 0°. When the PET substrate is set deflected to the right and left, respectively represent it as θ and θ^- (As shown in Fig. 1).

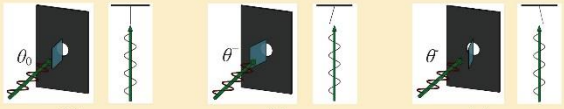

Fig. 1. Measurement of PET substrate inside TeraView TPS Spectra 3000.
(a) PET substrate parallel with propagation direction of the waves (θ = 0°);
(b) PET substrate deflected to right (+θ);
(c) PET substrate deflected to left (-θ).

Results

By rotating the mount when measuring the transmission spectrum, the signals of PET substrate in specific frequency will appear.

As shown in Fig. 2(a), when the angle of divergence with the PET, θ are 16° and -14°, a strong transmission dip appear in terahertz transmission spectrum. At this time, the frequency of terahertz spectrum are 0.6423 THz and 0.7271 THz, and the transmittance are -95.18 dB and -84.08 dB respectively.

Similarly, Fig. 2(b) shows the same experiment but changing the size of PET substrate to 2 cm × 3 cm. A transmission dip at 0.6059 THz and 0.6180 THz is measured, the transmittance at the dip are about -90.85 dB and -72.22 dB respectively. Each of them corresponding to different deflection angle which is θ= 8°10' and θ= -10°.

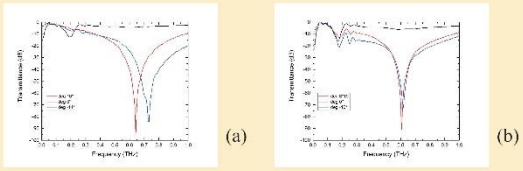

Fig. 2. Graph of Transmittance against Frequency for PET Substrate. In addition, the sizes of PET Substrate respectively are (a) 2 cm × 2 cm and (b) 2 cm × 3 cm.

Analysis

The transmission peaks of PET substrate 2 cm × 3 cm with θ= 8°10' and θ= -10° were overlapped, but this phenomenon do not appeared in the PET substrate of 2 cm × 2 cm.

As PET is birefringence material, optical axis of PET substrate can be fixed to perpendicular with propagation direction of the waves. In this situation, the frequency of transmission dips will overlap in θ and θ^-, as shown in Figure 3.

The phenomena in this study is due to the destructive interference of terahertz wave. In Fig. 1, the wave spot of 6 mm will split to two parts. The wave that pass through PET substrate will have a bigger optical path length than the wave didn't pass through. By rotating the mount as shown in Fig. 1(b) and Fig. 1(c), the optical path difference leads to destructive interference in specific frequency.

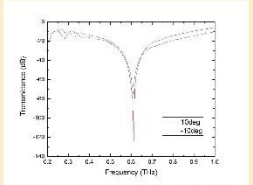

Fig. 3. Graph of Transmittance against Frequency for 2 cm × 3 cm fixed optical axis PET Substrate.

Conclusion and Discussion

In conclusion, the terahertz spectrum of the PET substrate with 2 cm × 2 cm and 2 cm × 3 cm had a transmission dip in specific deflection angle and specific frequency. A blue shift emerged when the long side of PET substrate increases. This characteristic of PET substrate is able to design a similarly high-performance band-stop filter at the terahertz regime which plays an important role in future's communications field.

液晶與超穎材料實驗室
Liquid Crystals and Metamaterials Laboratory
http://lcmm.thu.edu.tw/

Keywords: polyethylene terephthalate; deflected angle; terahertz

Exchange Bias in Co/OsMn films

M.R. Lin(林昅叡)[1], Y.W. Wang(王昱文)[1], C.R. Wang(王昌仁)[1], H.W. Chang(張晃暐)[1*]
[1]Department of Applied Physics, Tunghai University, Taichung 407, Taiwan

Introduction

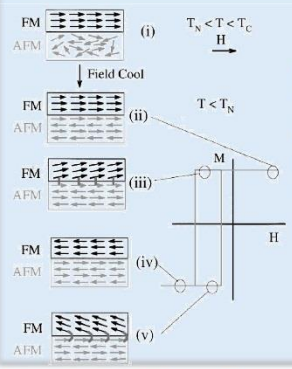

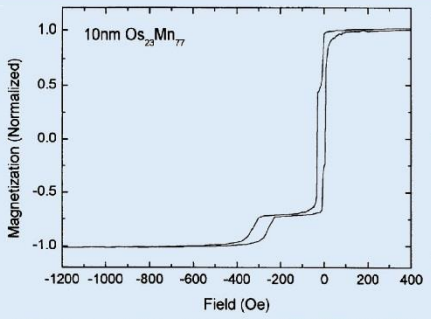

J. Nogués *et al.*, J. Magn. Magn. Mater., 192 (1999) 203-232
S.S.P.Parkin *et al.*, U.S. Patent No. 6,326,637 B1, (Dec. 4, 2001)

- Using heat treatment higher than Neel temperature with an external magnetic field along easy-axis and then cooling to room temperature is order to align magnetic dipole moments of antiferromagnetism (AFM) layer with ferromagnetism (FM) layer's.
- By field cooling treatment, a promoted exchange bias (EB) field was observed in some Mn-based AFM materials with high magnetocrystalline anisotropy such as PtMn. But limited report on magnetic properties of OsMn-based EB thin films is available.
- In this study, sputter-prepared Co/OsMn films were investigated. An as-deposited Ta/Co(5 nm)/OsMn(10 nm)/Ta film with **50 Oe Exchange Bias field** was observed without field cooling treatment. And more detailed study are under going.

Experiment methods

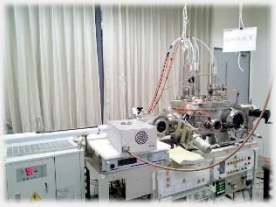

Ta
$OsMn(t_{AFM})$
$Co(t_{FM})$
Ta

AGM XRD AFM EDX

Results and discussion

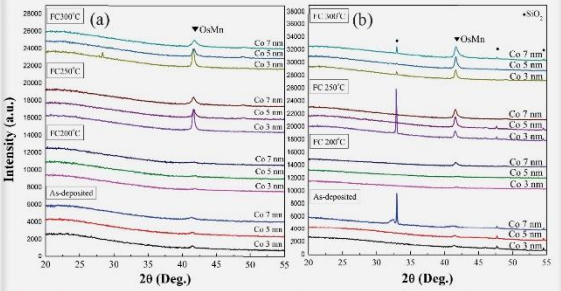

Fig. 1 XRD patterns of Ta(5 nm)/$Co(t_{FM})$/OsMn(30 nm)/Ta(5 nm) deposited on **(a)** glass and **(b)** SiO_2 substrates with various t_{FM} = 3, 5, 7 nm and field cooling temperature T_{FC} = 200℃, 250℃, 300℃.

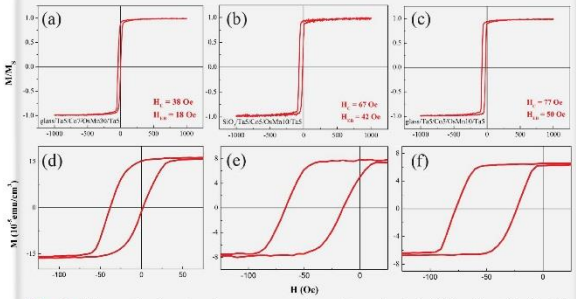

Fig. 2 Magnetic hysteresis curves of as-deposited **(a)(d)** glass/Ta/Co(7 nm)/OsMn(30 nm)/Ta **(b)(e)** SiO_2/Ta/Co(5 nm)/OsMn(10 nm)/Ta and **(c)(f)** glass/Ta/Co(5 nm)/OsMn(10 nm)/Ta films with high squareness (S > 0.9).

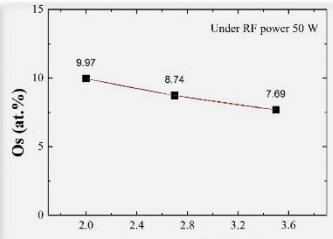

Fig. 3 Composition of Osmium (at.%) of OsMn films with Ar Pressure under RF power 50 W. The useful ranges of Osmium composition is reported to be from about 10 to 30 atomic %.

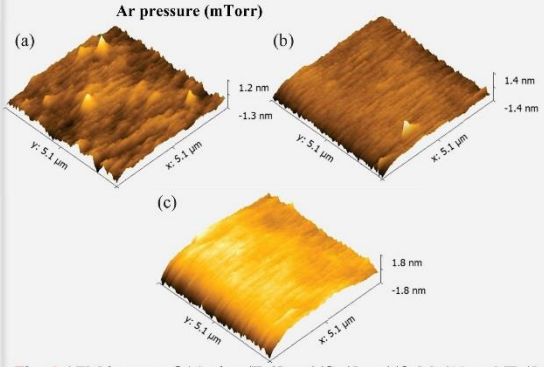

Fig. 4 AFM images of **(a)** glass/Ta(5 nm)/Co(5 nm)/OsMn(10 nm)/Ta(5 nm), **(b)** SiO_2/Ta(5 nm)/Co(5 nm)/OsMn(10 nm)/Ta(5 nm) and **(c)** glass/Ta(5 nm)/Co(7 nm)/OsMn(30 nm)/Ta(5 nm).

Conclusions

- In summary, exchange anisotropy phenomenon was observed in as-deposited Co/OsMn films with **50 Oe exchange bias field** and high squareness (S > 0.9). Those results contribute a new direction for choosing materials of spintronic devices. And this results are the only one data comparable with Parkin' s study.
- XRD patterns show a only one peak nearby 41°. Because of lacking of database of XRD analysis software, we are not able to discuss the texture before connecting with NSRRC(同步輻射中心).
- AFM images show that surface roughness is about 0.2 nm to 0.4 nm. And the higher roughness with lower squareness, that demonstrated the effect of roughness is important for properties of multilayer exchange bias films.

Structure and ferroelectric properties of $BiFeO_3$ films grown on CoPt/Pt bilayer buffered glass substrates

Y.C.Liu(劉育呈), H.W. Change(張晃暐)*, C.R. Wang(王昌仁)

Department of Applied Physics, Tunghai University, Taichung 407, Taiwan

I. INTRODUCTION

- Multiferroic $BiFeO_3$ with high remnant polarization about 100 μC/cm², high ferroelectric Curie temperature (T_C = 850 °C) and Neel temperature (T_N = 370 °C) have attracted increasing interests recently due to their fundamental physical properties and the potential applications in ferroelectric random-access memories (FeRAM) and magnetoresistive random-access memories (MRAM).
- Of all developed methods, RF sputtering has many advantages, including high reproducibility with an accurate stoichiometry and easy controlling process, and therefore it is considered as the most suitable way to prepare thin film with a smooth surfaces and dense structures. In this work, BFO thin films were prepared by RF magnetron sputtering.
- Since $L1_1$-CoPt phase with rhombohedral structure could form on proper Pt underlayer buffered glass substrates, BFO(111) texture is expected to obtained due to same crystal structure. Accordingly, structure and ferroelectric properties of $BiFeO_3$ films grown on CoPt/Pt bilayer buffered glass substrates have been studied.

II. EXPERIMENT

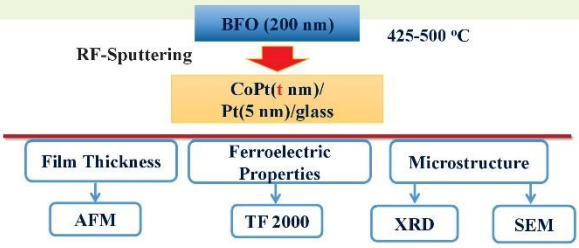

III. RESULTS AND DISCUSSION

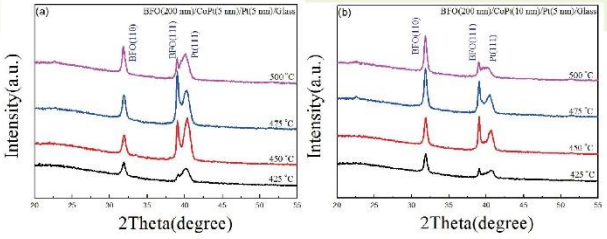

Fig. 1. XRD patterns of 200-nm-thick BFO thin films grown on CoPt/Pt/glass bilayer with different theik of bilayer and various annealing temperature. (a) 200-nm-thick BFO thin film grown on CoPt(5 nm)/Pt(5 nm)/glass. (b) 200-nm-thick BFO thin film grown on CoPt(10 nm)/Pt(5 nm)/glass.

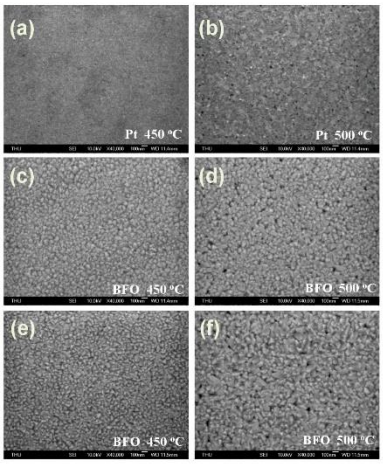

Fig. 2. SEM patterns of 200-nm-thick BFO thin films grown on CoPt/Pt/glass bilayer with different theik of bilayer and various annealing temperature. (a-b) SEM patterns of the Pt layer with various annealing temperature. (c-f) SEM patterns of 200-nm-thick BFO thin films grown on CoPt(5 nm)/Pt(5 nm)/glass bilayer and CoPt(10 nm)/Pt(5 nm)/glass with various annealing temperature.

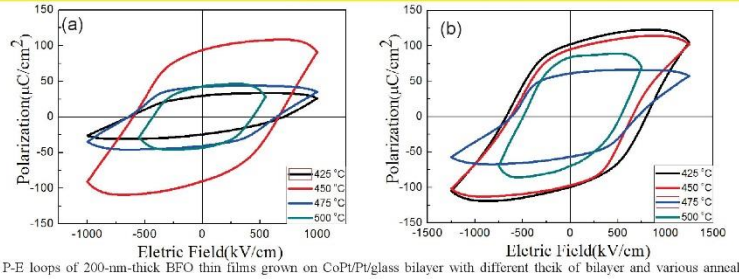

Fig. 3. P-E loops of 200-nm-thick BFO thin films grown on CoPt/Pt/glass bilayer with different theik of bilayer and various annealing temperature. (a)200-nm-thick BFO thin film grown on CoPt(5 nm)/Pt(5 nm)/Glass. (b) 200-nm-thick BFO thin film grown on CoPt(10 nm)/Pt(5 nm)/Glass.

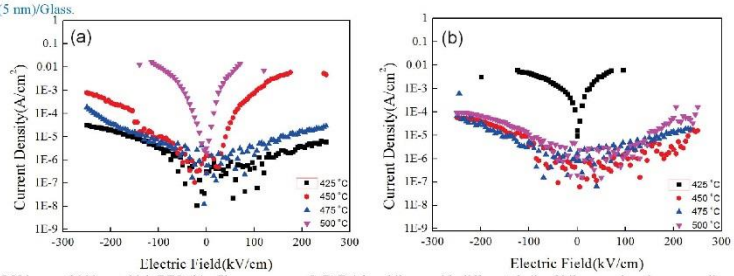

Fig. 4. J-V loops of 200-nm-thick BFO thin films grown on CoPt/Pt/glass bilayer with different theik of bilayer and various annealing temperature. (a) 200-nm-thick BFO thin film grown on CoPt(5 nm)/Pt(5 nm)/glass. (b) 200-nm-thick BFO thin film grown on CoPt(10 nm)/Pt(5 nm)/glass.

IV. CONCLUSIONS

- Single-phase 200-nm-thick BFO thin films grown on CoPt/Pt/glass substrates at various annealing temperature have been successfully prepared by rf sputtering.
- The orientation of BFO films is related to crystal structure of CoPt underlayer. All studied BFO films show a flat surface with dense and fine microstructure.
- Ferroelectric behavior with good properties ($2P_r$= 82-220 μC/cm²) and low leakage current are reached for the studied BFO films on CoPt/Pt underlayer at low temperature of 425-500 °C, which is beneficial for practical applications.
- Further study is needed and ongoing.

Anisotropic magnetoresistance in Ta/NiCo/Ta nanocrystalline thin films

P.F. Su[1](蘇品方), M.C. Chan[2](詹明哲), L.C. Kung[1](孔令丞), C.R. Wang[1](王昌仁),
D.H. Wei[2](魏大華), H.W. Chang[1,*](張晃暐)

[1]*Department of Applied Physics, Tunghai University, Taichung 407, Taiwan*
[2]Institute of Mechatronic Engineering, National Taipei University of Technology, Taipei 10608, Taiwan

Introduction

- The anisotropic magnetoresistance (AMR) of ferromagnetic alloys have attracted considerable attention for both the basic interest and technological applications in recent years.
- NiCo alloy has high anisotropic magnetoresistance (AMR) of 5%, but few report related to NiCo in thin films form is available.
- In this work, we investigate structure and MR properties of sputter-prepared Ta/$Ni_{100-x}Co_x$/Ta films (x=0-15) through proper post-annealing during the external magnetic field of 2 kOe.

Experiment

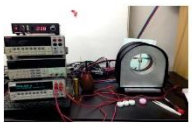

Ta(3nm)

$Ni_{100-x}Co_x$(20nm,0≤x≤15)

Ta(3nm)

SiO_2/Si(100)

Crystal structures by XRD | MR ratio by 4-point probe method | Surface morphology by AFM

Results and Discussion

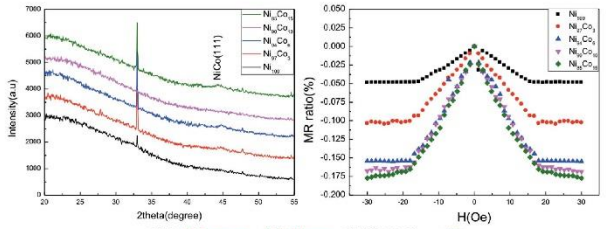

Fig 1. XRD patterns and MR-H curves of Ta/NiCo/Ta films at RT

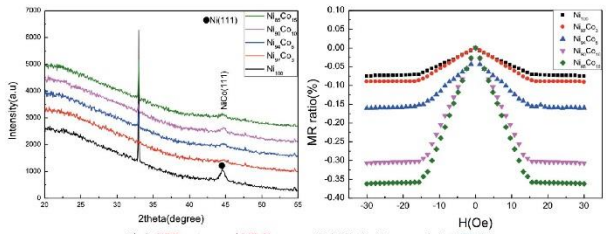

Fig 2. XRD patterns and MR-H curves of Ta/NiCo/Ta films annealed at 150°C.

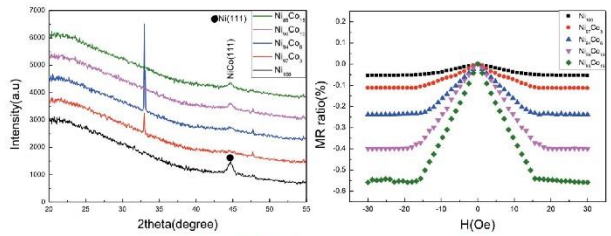

Fig 3. XRD patterns and MR-H curves of Ta/NiCo/Ta films annealed at 200°C.

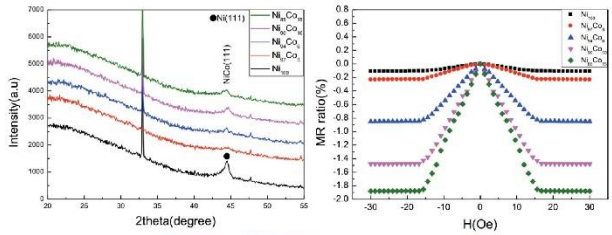

Fig 4. XRD patterns and MR-H curves of Ta/NiCo/Ta films annealed at 250°C.

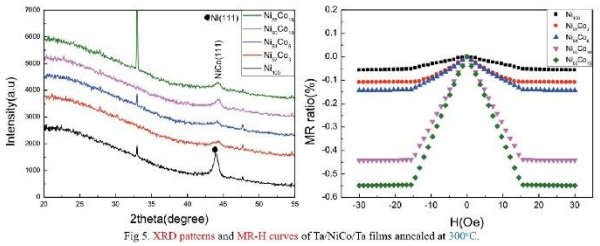

Fig 5. XRD patterns and MR-H curves of Ta/NiCo/Ta films annealed at 300°C.

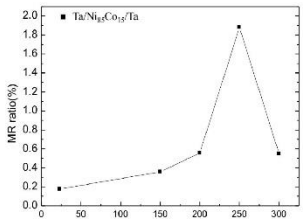

Fig 6. MR ratio under the different annealing temperature.

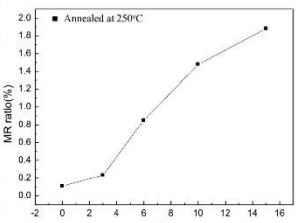

Fig 7. MR ratio of Ta/Ni100-xCox/Ta(x=0-15)

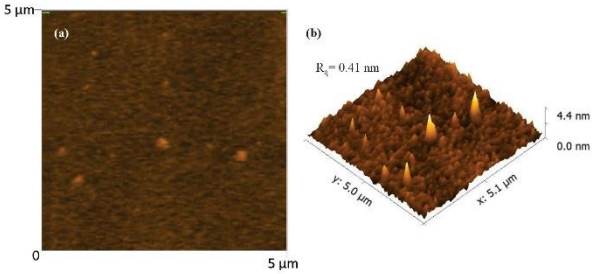

Fig 8. AFM images of Ta/$Ni_{85}Co_{15}$/Ta films annealed at 250°C (a)2D (b)3D

Conclusions

- Adjusting Co content and post-annealing temperature at magnetic field of 2 kOe can improve MR ratio.
- MR ratio increases with increasing Co content from 0 to 15 at%.
- Through post-annealing at 250 °C, Ta/NiCo/Ta reaches the maximum MR value of 1.9 % but exceed annealing 250°C, MR ratio is reduced because of interdiffusion between NiCo and Ta layers.
- Further study is ongoing!

Microstructure and ferroelectric properties of $BiFeO_3$ polycrystalline films with ZnO buffer layer

C.R. Huang(黃佳容), W.A. Chen(陳韋安), C.R. Wang(王昌仁), and H.W. Chang(張晃暐)*
Department of Applied Physics, Tunghai University, Taichung 407, Taiwan

Introduction

Of all developed multiferroic materials, BFO has attracted much attention due to its high both ferroelectric Curie temperature and antiferromagnetic Neel temperature, but the weak ferroelectric properties due to large leakage, limits the application.

The ferroelectricity of the oxide film is primarily determined by the choice of substrate / buffer layer and deposition technology etc.

ZnO is a piezoelectric wurtzite structure.

In this study, we use ZnO as a buffer layer to grow BFO film on Pt /glass substrates by sputter. In this work, structure, microstructure, and ferroelectric properties of the polycrystalline films prepared at various temperature are studied.

Experiment

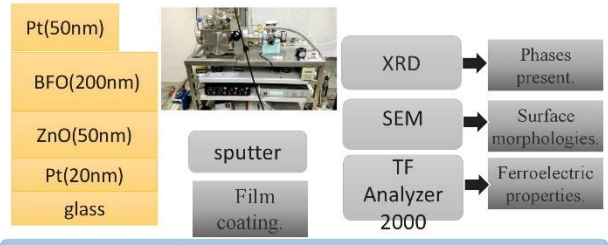

Results and discussion

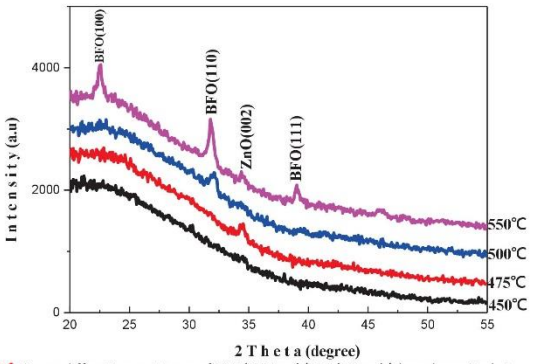

Fig1. X-ray diffraction patterns of BFO(200nm)/ZnO(50nm)/glass deposited at different temperatures.

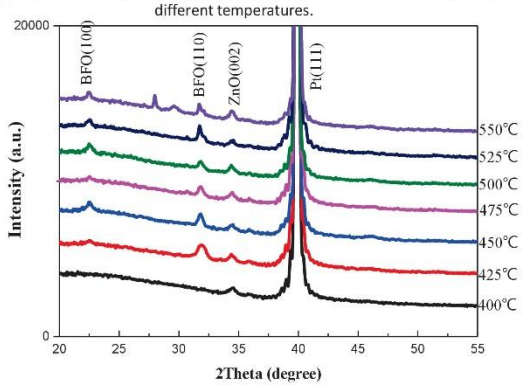

Fig2. X-ray diffraction patterns of BFO(200nm) / ZnO(50nm) / Pt(20nm) deposited at different temperatures.

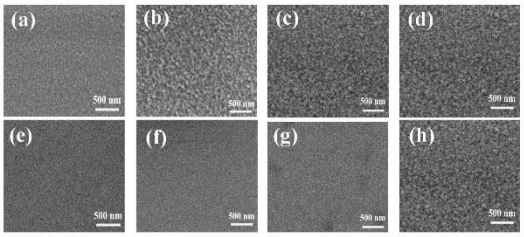

Fig3. SEM surface morphology patterns of BFO(200nm)/ ZnO(50nm)/glass at different temperature.
ZnO (a)at 450℃ ,(b)at 475 ℃ ,(c) at 500℃ ,(d)at 550 ℃
BFO (a)at 450℃ ,(b)at 475 ℃ ,(c) at 500℃ ,(d)at 550 ℃

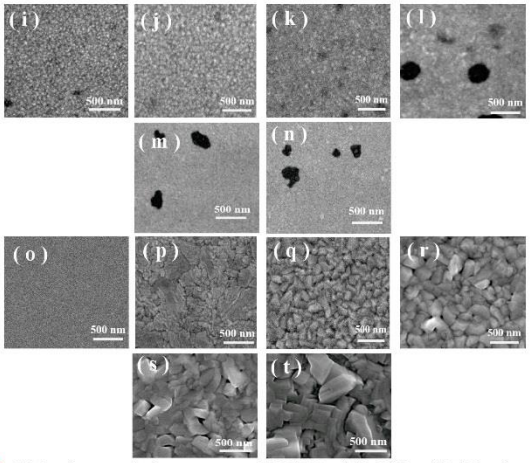

Fig4. SEM surface morphology patterns of BFO(200nm)/ ZnO(50nm)/Pt(20nm) at different temperature.
Pt (i)at 400℃ ,(j)at 425 ℃ ,(k) at 450℃ ,(l)at 500 ℃ ,(m)at 520℃ ,(n)at 550℃
BFO (o)at 400℃,(p)at 425 ℃ ,(q) at 450℃ ,(r)at 500 ℃ ,(s)at 520℃ ,(t)at 550℃

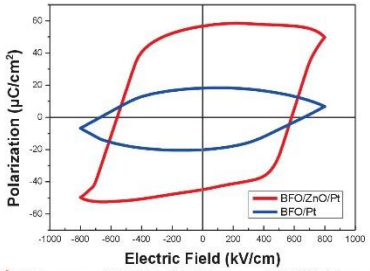

Fig4. P-E curves of BFO/ZnO/Pt/glass and BFO/Pt/glass at 450℃.

conclusions

- BFO films with pure perovskite phase have been successfully fabricated by sputter on buffer layer ZnO(002) at temperatures as low as 425–525 ℃.
- The studied BFO films on ZnO buffer layer exhibit a typical ferroelectric behavior with good properties of remanent polarization ($2P_r$) of 105 μC/cm² and electrical coercive field (E_c) is 560 (kV/cm).
- Further study is ongoing.

Detection of Hg^{+2} ions using liquid crystal cells with vertically aligning layers

Li-Yu Wu [1*] (吳俐諭), Yu-Hsuan Tsai [1] (蔡羽璇), Chih-Hsin Chen [2] (陳志欣), Chia-Yi Huang [1] (黃家逸)

[1]Department of Applied Physic, Tunghai University, Taichung, Taiwan
[2]Department of Chemistry, Tamkang University, New Taipei City, Taiwan

Abstract

A photoresist grid array is deposited on a glass substrate, and then a vertically aligning layer is coated on the array. The substrate with the vertically aligning layer is put in a drying cabinet at a relative humidity of 64 % and a temperature of 25 °C for 12 hours. After that, the mixture of a liquid crystal (LC) and a ligand is spin-coated on the substrate. As the LC sample is put in an optical microscope with crossed polarizers, the sample is at a dark state due to the vertical alignment. After a solution of Hg^{+2} ions is deposited on the LC layer, the sample is at a bright state. Such a sample can be used to detect Hg^{+2} in water.

Fabrication

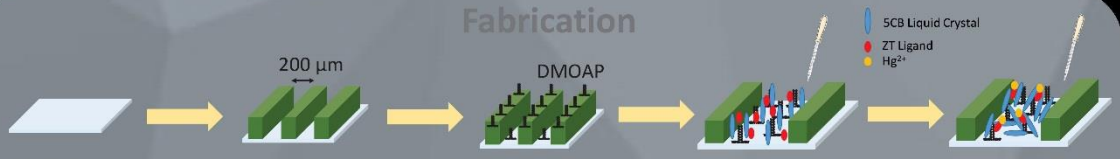

The ITO glass was cut to a size of 2.5 x 2.5 cm

A photoresist grid array is deposited on a glass substrate.

a vertically aligning layer is coated on the array.

the mixture of a 5CB liquid crystal (LC) and a ZT ligand is spin-coated on the substrate.

After a solution of Hg^{+2} ions is deposited on the LC layer, the sample is at a bright state.

Theory

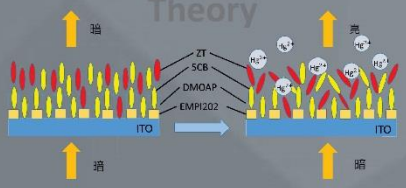

When the system was immersed in the solution containing Hg^{2+}, the complex of ZT and Hg^{2+} formed, which disrupted the orientation of LC and lead to a dark-to-bright transition of the image of LCs which is put in an optical microscope with crossed polarizers.

dark bright

Experiment

- Relative humidity of 50 %

24 hours 28 hours 32 hours 36 hours 48 hours

- Relative humidity of 64 %

8 hours 10 hours 13 hours 16 hours 24 hours

The image of samples which is put in an optical microscope with crossed polarizers,and smaples were put in a drying cabinet at different relative humidity and a temperature of 25 °C for several hours.

Conclusion

- The liquid crystal cell can be used to develop test strips for the determination of mercury(II) ion in aqueous samples. The test strips are compact, easy to operate and visible to naked eyes.
- Increasing the relative humidity of drying cabinet can decrease the time to appear better bright image.

Acknowledgments

The authors would like to thank the Ministry of Science and Technology of Taiwan for financially supporting this research under Contract No. MOST 104-2112-M-029 -004 -MY3

Optical Filters Based on Silver Nanoslits Embedded with Liquid Crystals

Yu-Hsuan Tsai[1*], Li-Yu Wu[1], Kuang-Li Lee[2], Pei-Kuen Wei[2], Chia-Yi Huang[1]
[1]Department of Applied Physics, Tunghai University, Taichung, Taiwan
[2]Applied Sciences, Research Center, Taipei, Taiwan
* presenting author:Yu-Hsuan Tsai, email:tstina0512@gmail.com

Abstract

The optical properties of the silver slits arise from surface plasma resonance (SPR), and the resonance frequency of the slits depends on the refractive indices of their surrounding media. The resonance wavelength of the test sample returns to its initial state after the removal of the voltages, so the tuning of the resonance wavelength is reversible. The experimental results depict that the silver slits embedded with the liquid crystal (LC) cell can be used to develop visible-light filters.

Fabrication

Interpret nanoslits on plastic substrate by hot pressing technique

Metallic film with a thickness of 120 nm is deposited on the plastic substrate

An empty cell comprises the substrate and an ITO glass on which a homogeneous aligned layer is coated. The empty cell is filled with LC

Application of voltages to an LC cell changes the refractive index of the LC. The spectrum of the nanoslits is blueshifted as visible light irradiates on the nanoslits. Therefore, the LC cell can be used to develop visible-light filters.

Experiment

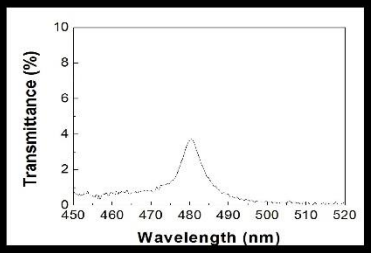

- Spectrum of LC cell with nanoslit's whose period ($\Lambda_{x(y),unit}$) is 470 nm

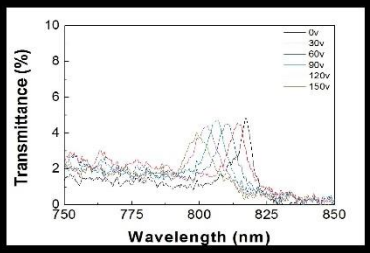

- The spectral blueshift arises from the fact that the LC director is oriented in a direction perpendicular to the substrate at 150 V.
- The spectrum of the LC cell with the silver nanoslits is reversible at the applied voltages

Spectra of LC cell with silver nanoslits whose period is Λ_{400nm} at various applied voltages.

Theory

✓ Surface plasmon resonance, SPR

According to the Maxwell Equation, only the Transverse magnetic mode (TM mode) can produce the SPR solution.

Maxwell equation

$\vec{B}_1 = (0, B_{y1}, 0)e^{i(k_{x1}x - k_{z1}z - \omega t)}$ (1)

$\vec{E}_1 = (E_{x1}, 0, E_{z1})e^{i(k_{x1}x + k_{z1}z - \omega t)}$ (2)

$\vec{H}_2 = (0, H_{y2}, 0)e^{i(k_{x2}x + k_{z2}z - \omega t)}$ (3)

$\vec{E}_2 = (E_{x2}, 0, E_{z2})e^{i(k_{x2}x + k_{z2}z - \omega t)}$ (4)

Substituting (1) to(4) into the $\nabla \times \vec{B}_j = \varepsilon_j \frac{1}{c^2} \frac{\partial \vec{E}_j}{\partial t} (j = 1,2)$

$k_{z1} H_{y1} = \varepsilon_1 \frac{\omega}{c^2} E_{x1}$ (5)

$k_{x1} H_{y1} = -\varepsilon_1 \frac{\omega}{c^2} E_{z1}$ (6)

$k_{x2} H_{y2} = -\varepsilon_2 \frac{\omega}{c^2} E_{z1}$ (7)

$k_{z2} H_{y2} = -\varepsilon_2 \frac{\omega}{c^2} E_{x2}$ (8)

SPR wave in this surface to meet the boundary conditions can be written as

$H_{y1} = H_{y2}$ (9)

$E_{x1} = E_{x2}$ (10)

$\varepsilon_1 E_{z1} = \varepsilon_2 E_{z2}$ (11)

Substituting (9) to(11) into the (5) to (8) can be obtained

$k_{z1} = k_{z2}$ (12)

$\frac{k_{x1}}{\varepsilon_1} = \frac{k_{x2}}{\varepsilon_2}$ (13)

The wavenumber in the medium can be written as

$k = \frac{\omega}{c} n = \frac{\omega}{c} \sqrt{\varepsilon}$ (14)

Thus in this system, the wavenumber can be written as

$k_x^2 = k_0^2 + k_{sp}^2 = \varepsilon_j \left(\frac{\omega}{c}\right)^2$ (15)

Substituting Eq. (13) into Eq. (15) gives the wave vector of the surface plasma wave

$k_{sp} = k_x = \frac{\omega}{c} \sqrt{\frac{\varepsilon_1 \varepsilon_2}{\varepsilon_1 + \varepsilon_2}}$ (16)

Eq. (16) is the conditions of produce SPR metal and dielectric substances.

✓ Nanoslit -excited surface plasmon resonance

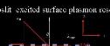

The level of the wave vector component at the interface is $k_{ix} = k_0 \sin\theta$

$k_{ix} = \frac{2\pi}{\lambda_0} \sin\theta \pm m \frac{2\pi}{\Lambda}$ (17)

When the wave vector in the horizontal direction of the light wave is equal to the wave vector of the surface plasma wave, so $k_{ix} = k_{sp}$

$k_{sp} = k_{0x}\sqrt{\varepsilon_1}$

So Eq. (18) can be simplified as

$\frac{2\pi}{\lambda_0} \sin\theta \pm m \frac{2\pi}{\Lambda} = k_{0x} \frac{\sqrt{\varepsilon_1 \varepsilon_2}}{\sqrt{\varepsilon_1 + \varepsilon_2}}$ (18)

$\frac{2\pi}{\lambda_0} \sin\theta \pm m \frac{2\pi}{\Lambda} = k_{0x}\sqrt{\varepsilon_1}$ (17)

Surface plasmon resonance occurred the most intense situation, so m=-1

$\frac{2\pi}{\lambda_0} \sin\theta = \frac{2\pi}{\Lambda} - k_{0x}\sqrt{\varepsilon_1}$ (18)

Let incident light perpendicular to the metal slit and $\theta = 0°$

$\frac{2\pi}{\Lambda} = k_{0x}\sqrt{\varepsilon_1}$ (19)

Substituting Eq. (19) k_0 change to $\frac{2\pi}{\lambda_0}$ and $\sqrt{\varepsilon_1}$ change to n_1 Eq of the dielectric material (18) can be rewritten as

$\lambda_0 = n_1 \Lambda$ (20)

Conclusion

- ✓ Application of voltages to the LC cell decreases the refractive index of the LC, blueshifting the transmission spectrum.
- ✓ The LC cell is an electrically controllable visible-light filter because the period of the nanoslits is 470 nm.
- ✓ If the peak transmittance and frequency tuning range of an LC cell with nanoslits are increased, the LC cell could be used to develop visible-light displays.

Acknowledgments

The authors would like to thank the Ministry of Science and Technology of Taiwan for financially supporting this research under Contract No. MOST 104-2112-M-029 -004 -MY3

Graphene quantum dots excited by different wavelengths

Ching-Feng Cheng, Tsong-Shin Lim

Department of Applied Physics, Tunghai University, Taichung 407, Taiwan

Abstract

在此研究中我們探討石墨烯量子點在不同激發脈衝的激發下，其發出的螢光之光譜和螢光生命週期有何影響。我們發現，石墨烯量子點的螢光光譜在不同波長的激發光(375 nm、432 nm、488 nm、532 nm)激發下並沒有明顯的變化。此外我們也發現其不同螢光波段的螢光生命週期幾乎都相同，而且在不同波長的激發光(432 nm、532 nm)激發下，其螢光生命期也都不變。目前我們所得到的結果與文獻上的結果完全不同，其詳細的原因還需做更進一步的探討。

Introduction

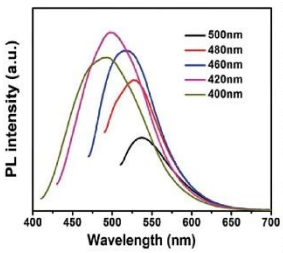

將石墨烯的尺寸縮小至奈米尺度形成石墨烯量子點(GQD)。石墨烯量子點具有能帶可以激發出穩定的螢光，且具有獨特的光學性質、低毒性、穩定的光致發光、化學穩定性、生物相容性，解決了石墨烯無法應用在生物細胞內的問題。因此可以做為細胞成像、藥物傳遞、生物傳感器多方面的應用。

石墨烯量子點的具有多種發光機制，因此，螢光光譜會隨著不同樣品製作、激發波長、溶液濃度而有所不同。本實驗所使用的是將樣品滴於固態基板中做不同激發波長對光譜的影響。

Experiment

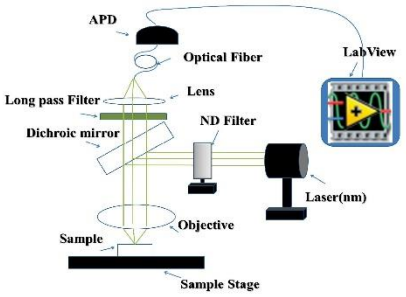

Conclusion

我們發現在不同波長的激發光激發下，GQD有著幾乎不變的螢光光譜以及螢光衰減曲線(螢光生命期)。我們的結果與目前文獻上所看到的結果完全不同。這有可能是因為樣品的狀態(文獻上的結果幾乎都是在溶液狀態下量測)，也有可能是因為樣品本身的純度所造成的。其詳細的原因還需再做進一步得探討。

Reference

1. *D. Pan , L. Guo , J. Zhang , C. Xi , Q. Xue , H. Huang , J. Li , Z. Zhang , W. Yu , Z. Chen , Z. Li , M. Wu , J. Mater. Chem. 2012 , 22 , 3314.*
2. *Fei Liu , Min-Ho Jang,Hyun Dong Ha , Je-Hyung Kim , Yong-Hoon Cho, and Tae Seok Seo. "Facile Synthetic Method for Pristine Graphene Quantum Dots and Graphene Oxide Quantum Dots: Origin of Blue and Green Luminescence"2013*

Results and Discussion

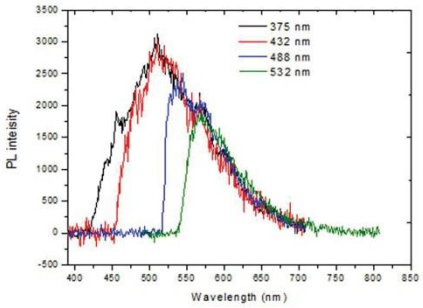

PL spectra of the GQDs at different excitation wavelengths

我們使用為不同的激發波長(375nm、432nm、488nm、532nm)做為激發光源量測GQD的螢光光譜。從上圖看來出螢光光譜的峰值似乎是隨著激發波長的增加而紅移。但是如果把每個激發光所使用的濾片的影響考慮進去，我們發現每一個螢光光譜有著相同的尾巴(沒有被濾片影響的部分)。這表示GQD的螢光光譜並沒有隨激發波長的改變而改變，這個結果跟文獻上的結果不太一樣。

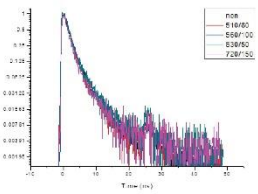

432nm pulse laser excitation

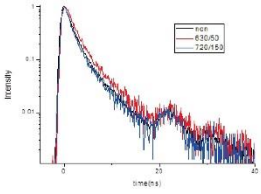

532nm pulse laser excitation

若不同的螢光波段來自於不同的發光機制，那不同的螢光波段將會有不同的螢光生命期。因此我們使用脈衝雷射激發，並使用不同的帶通濾片量測不同波段的螢光衰減曲線。上圖中我們分別使用了432 nm與532 nm的脈衝雷射激發，我們發現不同波段的螢光有幾乎相同的螢光衰減曲線。這表示所有波段的螢光都是來自於相同的發光機制。

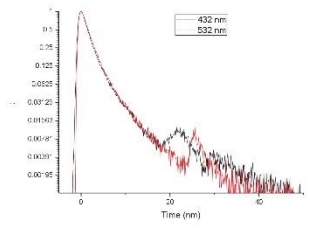

另外，若比較在不同激發光下的螢光衰減曲線，如上圖所示，我們發現兩條螢光衰減曲線也幾乎一模一樣。也就是說不同激發波長所激發出的螢光都是來自於同一個發光機制。這個結果跟文獻上所說的不同的激發波長會激發不同的發光機制，因而造成不同的螢光光譜以及不同的螢光衰減曲線完全不一致。

Magnetic Properties and Structure of IrMn/Co/Ta Thin Films

R.C. Yeh (葉柔辰)[1], C.R. Wang (王昌仁)[1], H.W. Change(張晃暐)[1*]

[1]Department of Applied Physics, Tunghai University, Taichung 407, Taiwan

Introduction

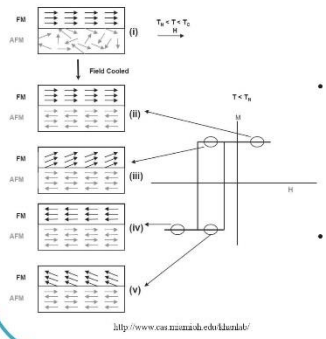

- IrMn has been identified as a promising antiferromagnetic material for advanced spintronic devices applications due to its high exchange coupling energy (J_k), high blocking temperature (T_b), and low critical thickness.
- In this present study, IrMn is adopted as a basic material, and structure and magnetic properties of sputtering-prepared IrMn/Co/Ta films at the external magnetic field of 1 kG induced by NdFeB sintered magnets at room temperature (RT).
- The magnetic properties of studied films are optimized by modification of working pressure during deposition of Ta(P_{Ta}), thickness of Ta(t_{Ta}), working pressure during deposition of IrMn(P_{IrMn}).

Experiment

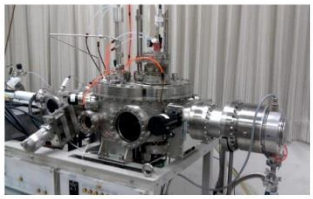

XRD

AFM

AGM

3 nm Ta	3 nm Ta	3 nm Ta
10 nm IrMn	10 nm IrMn	10 nm IrMn (x mTorr)
5 nm Co	5 nm Co	5 nm Co
Ta (t nm)	10 nm Ta (x mTorr)	10 nm Ta
SiO_2/Si(100)	SiO_2/Si(100)	SiO_2/Si(100)

Results and discussion

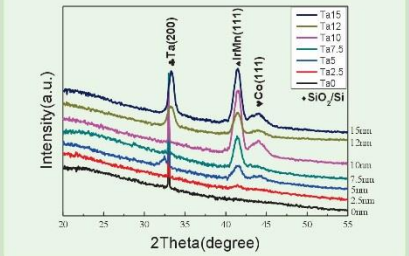

Fig. 1. XRD patterns of IrMn/Co/Ta with various thickness of Ta underlayer.

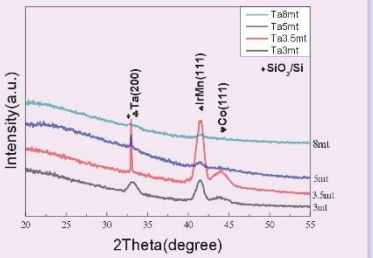

Fig. 4. XRD patterns of IrMn/Co/Ta with various working pressure of Ta underlayer.

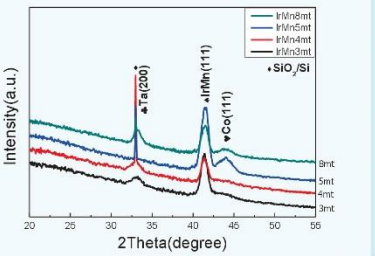

Fig. 7. XRD patterns of IrMn/Co/Ta with various working pressure of IrMn layer.

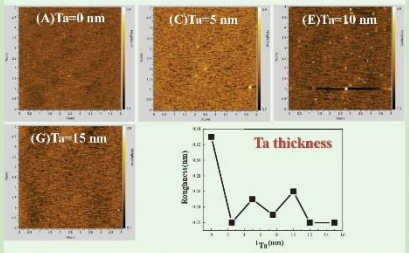

Fig. 2. AFM patterns of IrMn/Co/Ta with various thickness of Ta underlayer. (a) 0 nm, (b) 5 nm, (c) 10 nm, (d) 15 nm, of Ta underlayer.

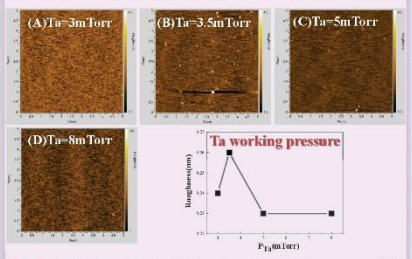

Fig. 5. AFM patterns of IrMn/Co/Ta with various working pressure of Ta underlayer. (a) 3 mTorr, (b) 3.5 mTorr, (c) 5 mTorr, (d) 8 mTorr, of Ta underlayer.

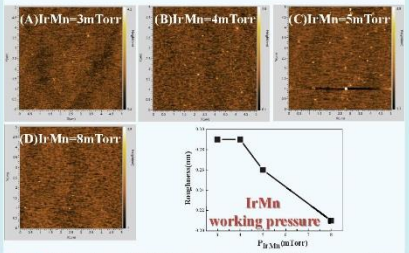

Fig. 8. AFM patterns of IrMn/Co/Ta with various working pressure of IrMn underlayer. (a) 3 mTorr, (b) 4 mTorr, (c) 5 mTorr, (d) 8 mTorr, of IrMn underlayer.

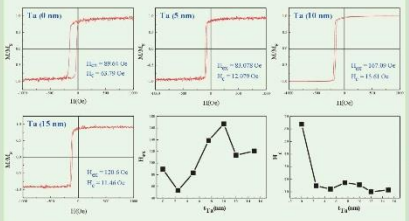

Fig. 3. M-H curves patterns of IrMn/Co/Ta with various thickness of Ta underlayer. (a) 0 nm, (b) 5 nm, (c) 10 nm, (d) 15 nm, of Ta underlayer.

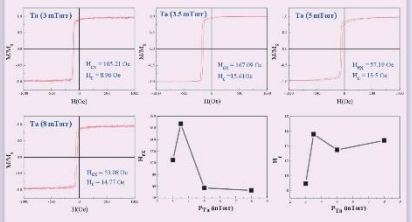

Fig. 6. M-H curves patterns of IrMn/Co/Ta with various working pressure of Ta underlayer. (a) 3 mTorr, (b) 3.5 mTorr, (c) 5 mTorr, (d) 8 mTorr, of Ta underlayer.

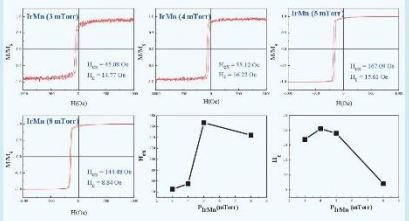

Fig. 9. M-H curves patterns of IrMn/Co/Ta with various working pressure of IrMn underlayer. (a) 3 mTorr, (b) 4 mTorr, (c) 5 mTorr, (d) 8 mTorr, of IrMn underlayer.

Conclusons

- The adoption of a proper Ta seed layer is effection in strengthing IrMn(111) texture and therefore optimizing exchange-bias field, in IrMn/Co system.
- The optimized exchange bias field (H_{ex}) of 167.1 Oe with very small coercivity (H_c) of 15.6 Oe obtained due to good crystallinity of IrMn(111) and flat interface between IrMn and Co layers is better than the same system reported by other group (Y.-T. Chen et al., Journal of Alloys and Compounds 509 (2011)、Z.B. Guo et al., Solid State Communications 147 (2008)).
- Further study is ongoing.

Exchange bias in Co/MnPt polycrystalline films on SiO_2/Si(100) substrates

P.H. Pan(潘柏亨)[1], H.W. Change(張晃暐)[1*], C.R. Wang(王昌仁)[1], Lance Horng (洪連輝)[2]

[1] Department of Applied Physics, Tunghai University, Taichung, 407 Taiwan.
[2] Department of Physics, National Changhua University of Education, Changhua 500, Taiwan.

Introduction

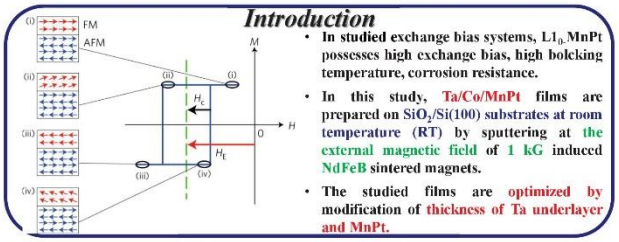

- In studied exchange bias systems, $L1_0$-MnPt possesses high exchange bias, high bolcking temperature, corrosion resistance.
- In this study, Ta/Co/MnPt films are prepared on SiO_2/Si(100) substrates at room temperature (RT) by sputtering at the external magnetic field of 1 kG induced NdFeB sintered magnets.
- The studied films are optimized by modification of thickness of Ta underlayer and MnPt.

Experiment

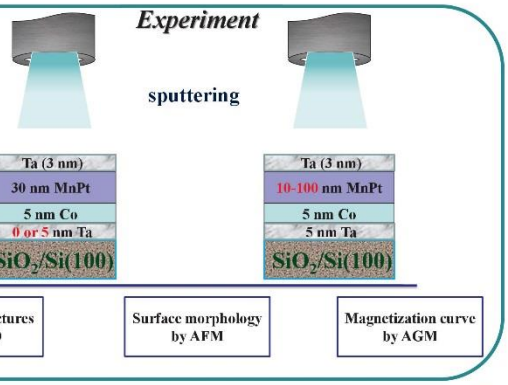

Results and Discussion

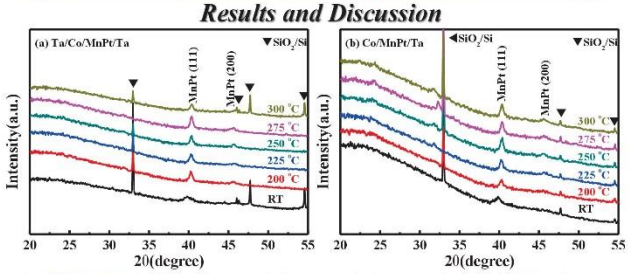

Fig.1. XRD patterns of Co/MnPt bilayer deposited on various Ta thickness (a) 5 nm and (b) 0 nm with various annealing temperature.

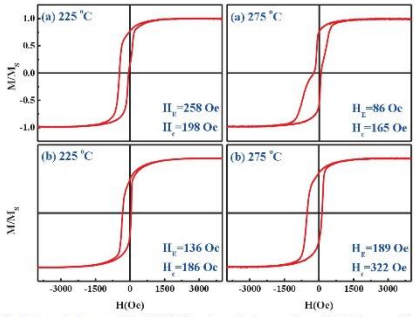

Fig.2. Magnetic hysteresis loops of Co/MnPt film deposited on various Ta thickness (a) 5 nm and (b) 0 nm with various annealing temperature.

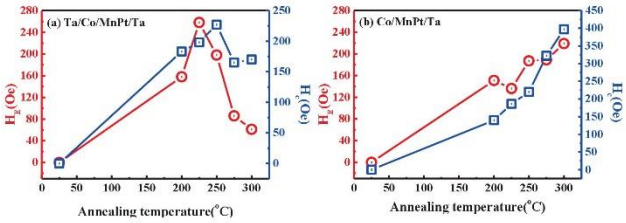

Fig.3. Dependence of H_{eb} and H_c on annealing temperature with various Ta thickness (a) 5 nm and (b) 0 nm .

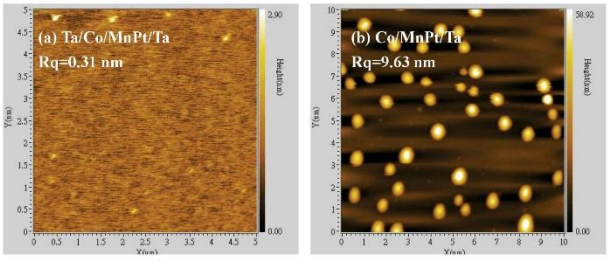

Fig. 4. AFM images of annealing temperature 275 °C with various thickness of Ta underlayer (a) 5 nm and (b) 0 nm

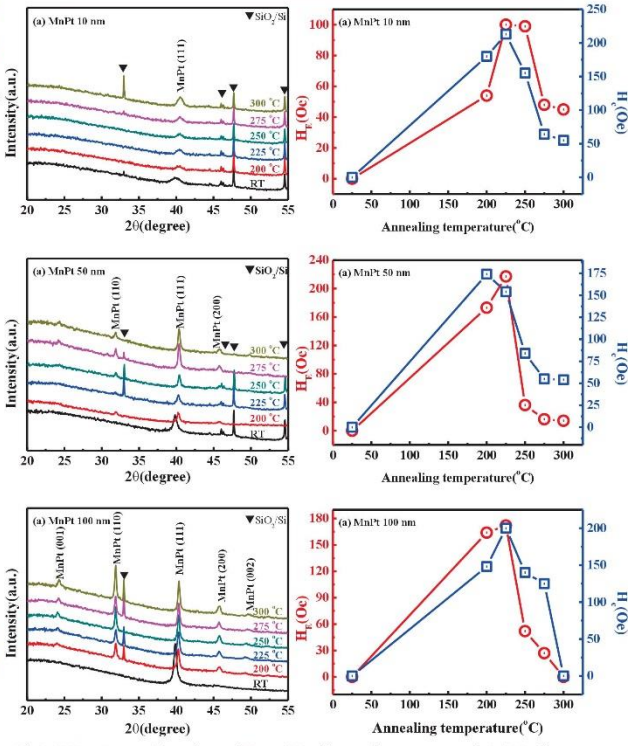

Fig.5. XRD patterns and dependence of H_{eb} and H_c with annealing temperature of Co/MnPt film deposited on various Ta thickness (a) 5 nm and (b) 0 nm .

Conclusions

1. The largest H_{eb} of 258 Oe is obtained in the presented Ta/Co/MnPt(30 nm) films by sputtering at the external magnetic field with 5 nm thickness of Ta underlayer and 275 °C of annealing temperature, and it accompanies a small H_c of 198 Oe.
2. Flatter surface of Co/MnPt deposited on Ta underlayer is obtained.
3. The strengthened diffraction intensity of MnPt (111) and the presence other diffraction peaks with MnPt thickness reveal enhanced $L1_0$-ordering in MnPt layer.
4. Larger H_c than H_E obtained in 10-nm-thick MnPt results from larger exchange interaction energy between the Co and MnPt than anisotropy energy of MnPt.

Texture control of $BiFeO_3$ films on glass substrates with CoPt electrode underlayers

C.C. Liu[1](劉佳蒨), C.R. Wang, H.W. Chang*

Department of Applied Physics, Tunghai University, Taichung 407, Taiwan

Introduction

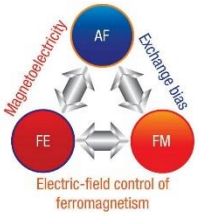

Multiferroic $BiFeO_3$ (BFO) exhibits both a ferroelectric phase transition at the high Curie temperature and a magnetic phase transition at the Néel temperature. BFO thin films possesses a large polarization value and low crystallization temperature, both of which are desirable properties for applications in high density ferroelectric random access memories (FeRAMs) and advanced spintronic devices. In this study, BFO films are grown on CoPt(111) underlayer on glass substrate by sputtering. In addition to serving as a FM bottom electrode, CoPt(111) is also expected to obtain different orientation of the film.

Experiment

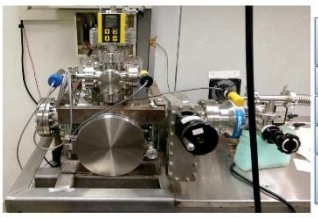

BFO (150 nm)
CoPt(111) (5 nm)
Pt (10 nm)
Ta (5 nm)
glass

BFO (150 nm)
CoPt(111) (5 nm)
glass

XRD | TEM | TF Analyzer 2000 | VSM

Results and discussion

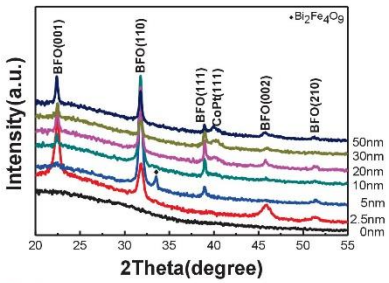

Fig. 1 XRD patterns of 200-nm-thick BFO films grown on various thickness of CoPt(111) buffered on glass substrates.

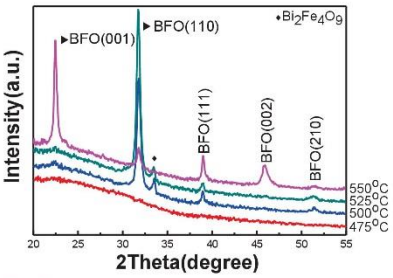

Fig. 2 XRD patterns of 200 nm $BiFeO_3$ films grown on CoPt/glass substrate with various temperatures

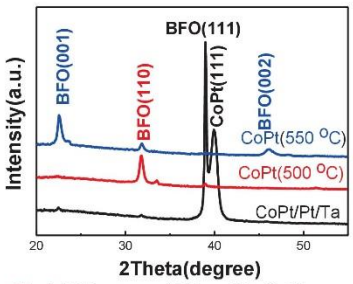

Fig. 3 XRD patterns of 200 nm $BiFeO_3$ films grown on glass substrate with different underlayers.

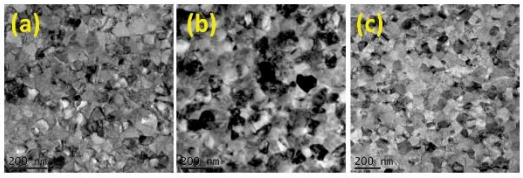

Fig. 4 TEM images of 200 nm $BiFeO_3$ films grown on glass substrate at T_g = 500 °C with different underlayers (a) CoPt (550 °C), (b) CoPt (500 °C), (b)CoPt/Pt/Ta

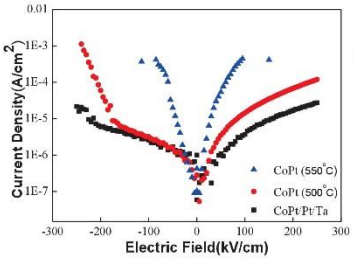

Fig. 5 J-E Curves of 200 nm $BiFeO_3$ films grown on glass substrate with different underlayers.

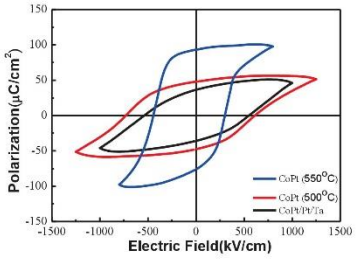

Fig. 6 P-E Curve of 200 nm $BiFeO_3$ films grown on glass substrate with different underlayers.

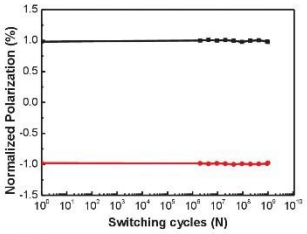

Fig. 7 Fatigue behavior of $BiFeO_3$ films grown on CoPt(5 nm)/glass substrate at 500 °C.

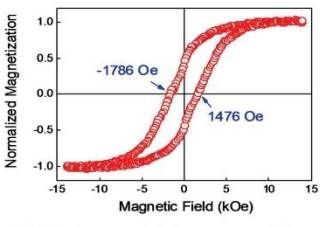

Fig. 8 In-plane M-H curves of 200-nm-thick BFO films grown on CoPt(111) buffered on glass substrates at T_d=450°C.

Conclusions

- All textures of $BiFeO_3$ films on glass substrates with CoPt underlayers have been successfully controlled: **(110) and (001) orientations for CoPt(111) at 500 and 550 °C; (111) for CoPt/Pt/Ta**, respectively.
- The ferroelectric properties are related to texture of BFO: BFO(111) film shows the highest polarization, while the (100)-oriented BFO(001) film possesses an almost fatigue-free behavior.
- The exchange bias between BFO and CoPt is observed for the optimized sample after a field cooling from 370°C to RT at 2 kOe, and large exchange bias field of 155 Oe at RT and coercivity of 1631 Oe are obtained.
- The presented results provide useful information for the applications based on electric-magnetic interactions.

Effect of Ti underlayer on structure and magnetic properties of rapid thermal annealed FePt thin films

C.L. Fan (范振琳)[1], C.Y. Shen (申繼陽)[2], M.C. Lin (林明忠)[1], Y.W. Wang (王昱文)[1], H.W. Chang (張晃暐)[1*]

[1] Department of Applied Physics, Tunghai University, Taichung, 407 Taiwan.
[2] Department of Electrical Engineering, Hsiuping University of Science and Technology, Taichung.

Introduction

FePt alloy with $L1_0$ structure is one of the most studied materials due to excellent corrosion resistance and magnetically intrinsic properties, including strong uniaxial magnetocrystalline anisotropy, large saturation magnetization, and high Curie temperature.

Many studies focused on the optimization of hard magnetic properties for the potential applications in the micro-electro-mechanical systems (MEMS)

Inducing strong intergrain coupling and introducing soft magnetic phase with higher magnetization in hard magnetic matrix to form strong exchange coupling are two efficient ways to maximize the energy product, $(BH)_{max}$, an index denoting the energy density that a permanent magnet stored.

In order to further reduce the grain size to strengthen the intergrain coupling, ordering must be triggered at lower temperatures to suppress grain growth induced by phase transformation.

In this work, Ti underlayer is adopted to enhance the magnetic properties of FePt films and significant increase in $(BH)_{max}$ is achieved.

Experiment

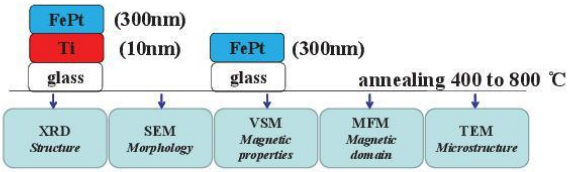

Results and Discussion

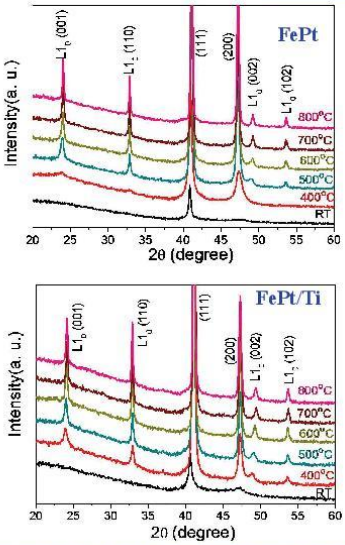

FIG. 1. XRD patterns of the FePt and FePt/Ti films at various post-annealing temperatures.

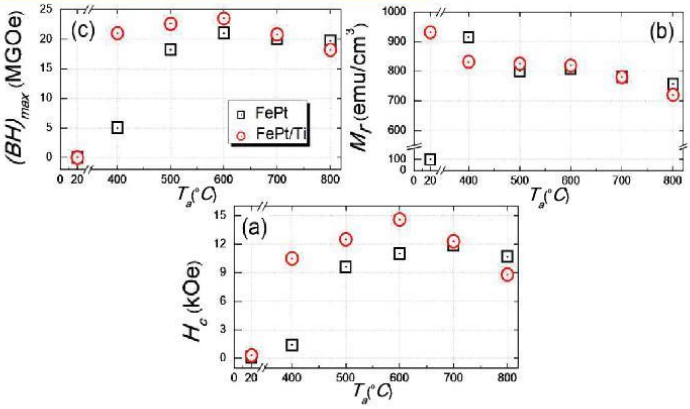

FIG. 4. Magnetic properties of the FePt and FePt/Ti films at various post-annealing temperatures.

FIG. 2. SEM images of the FePt and FePt/Ti films at various post-annealing temperatures.

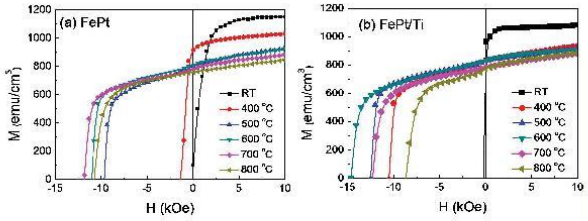

FIG. 3. M-H curves images of the FePt and FePt/Ti films at various post-annealing temperatures.

FIG. 5. TEM images of the FePt and FePt/Ti films post annealed at 600 ℃ and 800 ℃.

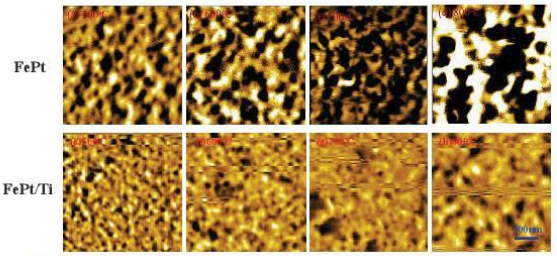

FIG. 6. MFM images of the FePt and FePt/Ti films post annealed at 500 ℃ to 800 ℃.

Conclusions

- Structure and magnetic properties of FePt (300 nm) and FePt(300 nm)/Ti(10 nm) films are studied.
- The low temperature ordering of FePt with Ti underlayer reduces grain growth and thus enhances the intergrain coupling.
- Significant enhancement is achieved in the Ti-underlayered samples.
- The value of $(BH)_{max}$ for the Ti-underlayered films with T_a = 400-700°C are 21.0-23.5 MGOe.
- The presented results confirm that using Ti as an underlayer not only lowers the onset point of $L1_0$-ordering but also enhances the permanent magnetic performance.

Acknowledgements

This research was financially supported by Ministry of Scienceand Technology of Taiwan, under grant No. MOST-103-2112-M-029-001.

Magnetic properties and nanostructures of Fe-rich FePt films

Y.C. Wang(王翊臻), H.W. Change(張晃暐)*, C.R. Wang(王昌仁)

[1]Department of Applied Physics, Tunghai University, Taichung 407, Taiwan

I. INTRODUCTION

FePt alloy with $L1_0$ structure is one of the most studied materials for applications in the bio-magnets on dentistry and micro-electro-mechanical (MEMS) due to strong uniaxial magnetocrystalline anisotropy (K_u = 7x10^7 erg/cm^3), high Curie temperature (T_C ~ 450 °C), large saturation magnetization($4\pi M_s$) and excellent corrosion resistance. The former two intrinsic properties leads to the size of $L1_0$-FePt alloy down to several nanometer having good thermal stability.

Most studies are concentrated on the vicinity of the $Fe_{50}Pt_{50}$. To date, rare study on the compositions between $L1_0$ and $L1_2$ phase, Fe_xPt_{100-x} (x = 66-73), is available. Besides, the magnetization of FePt alloy may be enhanced if the composition in this region is adopted.

In this study, high vacuum sputtering system is used to prepare Fe_xPt_{100-x} (x = 66-73) films on glass substrate. Effect of composition and post annealing temperature on the magnetic properties, structure and microstructure of Fe_xPt_{100-x} (x = 66-73) are studied.

II. EXPERIMENT

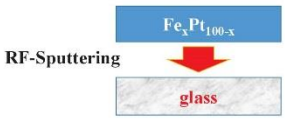

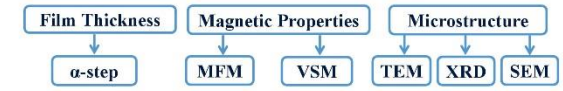

III. RESULTS AND DISCUSSION

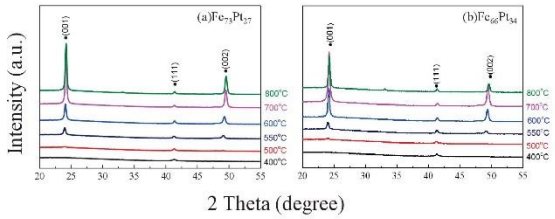

Fig. 1. XRD patterns of 30-nm-thick FePt thin films grown on glass substrate with various annealing temperature. **When the annealing temperature ranges from 400 to 800 °C for 10 min, $L1_0$-ordering occurs. High (001) preferred orientation is obtained at higher temperature (600-800 °C).**

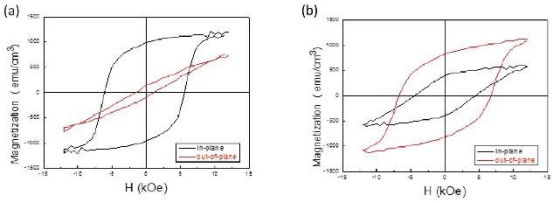

Fig. 2. and Fig. 3. SEM images and M-H curves of FePt thin films grown on glass substrate with annealing 600 °C. (a)$Fe_{72}Pt_{27}$(b)$Fe_{66}Pt_{34}$. **SEM results show that fine microstructure and grain size of 50-100nm are observed. It is worthy to mention that the magnetic properties of $(BH)_{max}$ 13.4 MGOe and H_c = 2.2 kOe can be attained for $Fe_{66}Pt_{34}$ films post annealed at 400 °C, and $(BH)_{max}$ = 28.4 MGOe and H_c = 5.7 kOe can be attained for $Fe_{66}Pt_{34}$ films post annealed at 600 °C.**

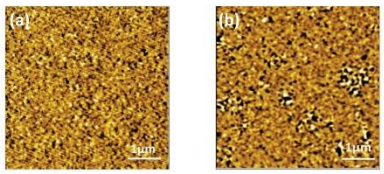

Fig. 4. MFM images of FePt thin films grown on glass substrate annealed at 600 °C. (a)$Fe_{73}Pt_{27}$(b)$Fe_{66}Pt_{34}$. **The magnetic domain is bigger than its grain size, an indicative of the interaction domain.**

TEM images of $Fe_{73}Pt_{27}$ films

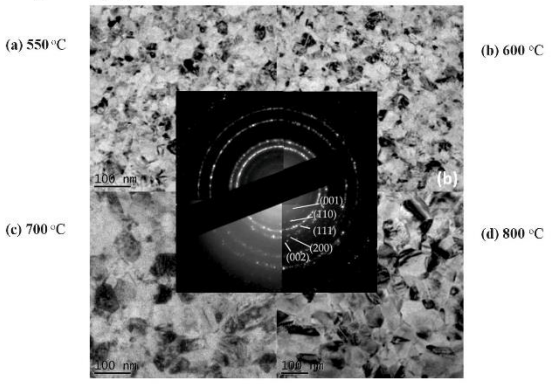

TEM images of $Fe_{66}Pt_{34}$ films

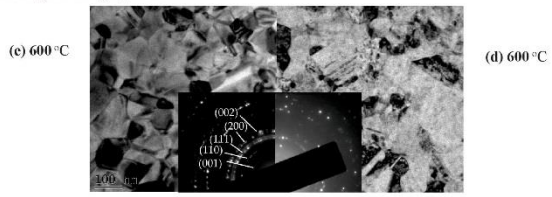

Fig. 5 .**The grain size is increased with annealing temperature.**

IV. CONCLUSIONS

- **In this study, Fe_xPt_{100-x} (x = 66-73) films with (001)-texture on glass substrate have been successfully prepared by sputtering.**
- **A1 phase is present for as-deposited Fe_xPt_{100-x} (x = 66-73) films.**
- **When the annealing temperature ranges from 400 to 800 °C for 10 min and the heating rate is fixed at 40 °C/s, $L1_0$-ordering occurs.**
- **High (001) preferred orientation is obtained at higher temperature (600~800 °C).**
- **$Fe_{72}Pt_{27}$ has an in-plane magnetic anisotropy, while $Fe_{66}Pt_{34}$ has an out-plane magnetic anisotropy.**
- **The grain size is increased with annealing temperature.**
- **The optimal magnetic properties of $(BH)_{max}$ = 28.4 MGOe and H_c = 5.7 kOe can be attained for $Fe_{66}Pt_{34}$ films post annealed at 600 °C.**
- **Further study is needed and ongoing.**

Effect of Ca substitution on the multiferroic properties of $BiFeO_3$ films on glass substrates at reduced temperature

S.Y. Lin (林恩妤)[1], Y.C. Lo (羅宇棋)[1], K.T. Tu (涂凱騰)[1],
C.R. Wang (王昌仁)[1], C.S. Tu (杜繼舜)[2], H.W. Chang (張晃暐)[1*]

[1]Department of Applied Physics, Tunghai University, Taichung 407, Taiwan
[2]Department of Physics, Fu Jen Catholic University, Taipei 242 Taiwan

I. INTRODUCTION

Perovskite $BiFeO_3$(BFO), showing outstanding multiferroic(MF) properties of ferroelectricity (FE) (T_C ~810 C) and antiferromagnetism (AFM)(T_N~370 C),has recently received considerable attention. However, a G-type AFM order with a spatially modulated spin structure in bulk-BFO cancels out any possible net magnetization and thus hinders the applications.

$Bi_{1-x}Ca_xFeO_3$(BCFO) was reported showing interesting structural, magnetic, and electrical evolutions and a significant photovoltaic effect. Moreover, a converse magnetoelectric effect was observed in BCFO ceramics, but very low electrical remanent polarization ($2P_r$) of 0.4–8 μC/cm² hinders the applications.

In this work, BCFO films with x = 0.05, 0.1, and 0.15 are grown on refined metallic Pt(111) electrode layer buffered glass substrate by pulsed laser deposition (PLD) at reduced temperature of 450°C. Structural, ferroelectric, and magnetic characterizations of BCFO films are reported.

II.EXPERIMENT

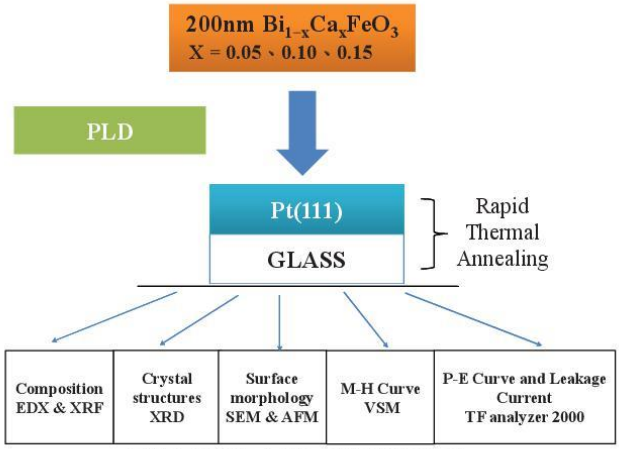

III.RESULT AND DISCUSSION

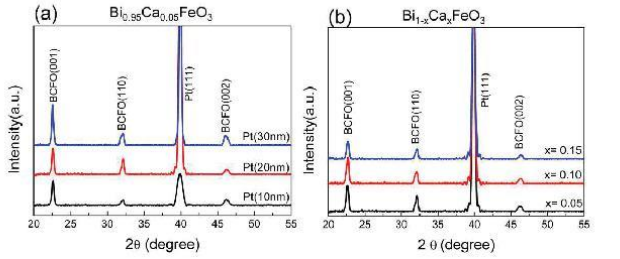

FIG. 1. XRD patterns of (a) $Bi_{1-x}Ca_xFeO_3$ films grown on various Pt thicknesses (b) $Bi_{1-x}Ca_xFeO_3$ films grown on various Pt /glass substrates.

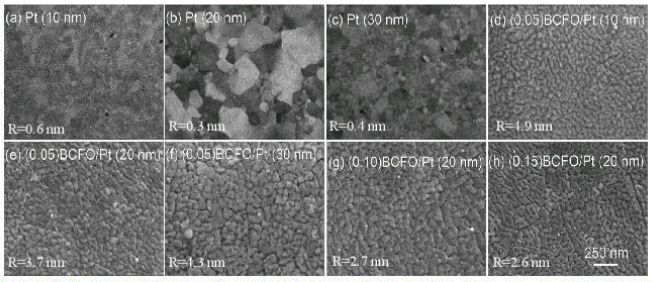

FIG. 2. SEM images of Pt layer with various thicknesses and $Bi_{1-x}Ca_xFeO_3$ films grown on various Pt/glass substrates.

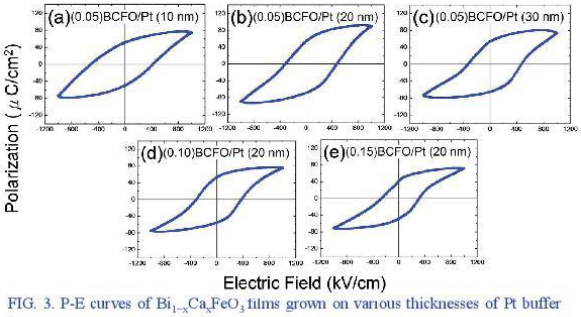

FIG. 3. P-E curves of $Bi_{1-x}Ca_xFeO_3$ films grown on various thicknesses of Pt buffer layer.

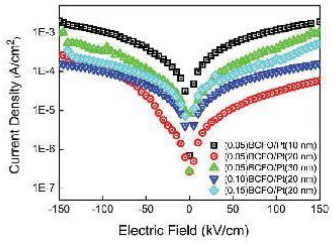

FIG. 4. Leakage current density as a function of the external electric field for $Bi_{1-x}Ca_xFeO_3$.

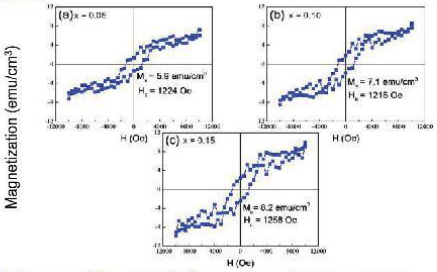

FIG. 5. M–H curves of $Bi_{1-x}Ca_xFeO_3$ films grown on Pt /glass substrates.

IV . CONCLUSIONS

- Structure, surface morphology, ferroelectric and magnetic properties of Ca-doped BFO films prepared by pulsed laser deposition on Pt bottom electrodes with various t buffered glass substrates at low substrate temperatures of 450 °C have been examined.
- The structural analysis shows that a pure perovskite phase with the isotropic orientation is present for BCFO films with x = 0.05–0.15 and t = 10–30 nm.
- Grain size and surface morphology of the BCFO films are sensitive to the configuration of Pt(1 1 1) layer, and besides, the grain size and surface roughness of BCFO films are reduced with increasing Ca content.
- Different from poor ferroelectric properties for BCFO ceramics, the studied BCFO polycrystalline films exhibit typical multiferroic properties comparable to BFO films grown on single crystal substrates.
- The ferroelectric properties are sensitive to microstructure, surface morphology, and Ca content. The good ferroelectric properties with the remanent polarization ($2P_r$) of 91–124 C/cm²and electrical coercive field (E_c) of 294–394 kV/cm are obtained for BCFO films with x = 0.05–0.15 and t = 10–30 nm owing to fine microstructure, flat surface, and low leakage current.
- All studied BCFO films exhibit a ferromagnetic behavior with M_s= 5.9–8.2 emu/cm³and H_c= 1224–1258 Oe due to the suppressed spiral spin configuration of AFM in BFO by a substitution of Ca^{2+}.
- The results of this study reveal that polycrystalline BCFO films on fine controlled Pt electrode on glass substrate with reduced formation temperature could be a highly potential multiferroic material for advanced applications.

Acknowledgements

This research was financially supported by Ministry of Scienceand Technology of Taiwan, under grant No. MOST-103-2112-M-029-001.

Electronically Controllable Terahertz Filters Using Electrowetting-On-Dielectric Cells With Metamaterial

Yu-Shao Chen(陳昱劭) and Chia-Yi Huang*(黃家逸)
*chiayihuang@thu.edu.tw
Department of applied physics, TUNGHAI UNIVERSITY, Taichung, Taiwan

Abstract

A metamaterial that is embedded in glycerin droplet or air is controlled by voltage. which is used to develop passively tunable terahertz devices such as filters, absorbers, sensors, and spectral imagers. The resonance peak of the metamaterial can be redshifted as the metamaterial "experiences" an increase in the refractive index of a medium that surrounds it. A simulation confirms the spectral redshift and the refractive index of glycerin (n=1.47). The variation in peak frequency are depended on the position of glycerin. Experimental results show that the resonance peak of the metamaterial can be continuously tuned within a frequency range of 0.25 THz as the droplet moving by applied voltage 120 V. Therefore, this metamaterial is a continuously tunable and exhibits a higher frequency tuning range than other liquid crystal cells with metamaterials.

Experimental

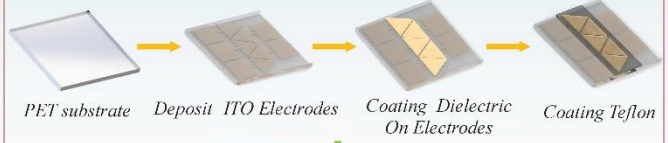


EWOD Cell

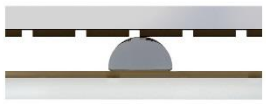
EWOD Cell's Cross Section

Theory

◆ Electrowetting-on-dielectric

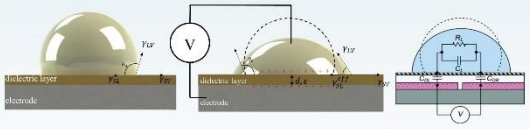

◆ Surface Plasmon Resonance

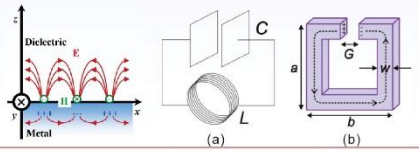

Simulation

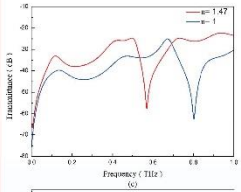

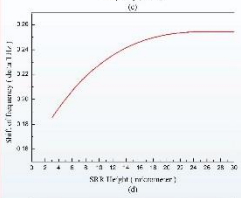

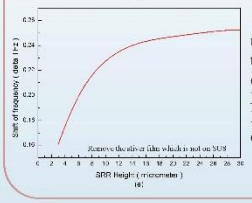

A simulation is performed using commercial finite-difference time-domain software to verify the experimental results in the Fig. (c). The experimental spectra in Fig. (a) match the simulated spectra in Fig. (c).

This cell has a limitation in its frequency tunable range. To find the limit, we did the two series of simulation that are presented in Fig. (d) and Fig. (e). The x-axis is the height of SRR, the y-axis is shift of frequency. As the height of SRR small than 18 μm, the shift of frequency are increasing. But the data lines tend to 0.25 delta THz when height are large than 18 μm. Obviously, this device has a limit at frequency tunable range. Therefore, the height of SRR have a best value when it equal 18 μm.

The different of Fig. (d) and Fig. (e) are transmittance. Because of the silver film on the substrate (show in Experimental) will decay the transmittance of THz. To compare Fig. (d) & (e), the tunable range have same limit. That is to say, Fig. (e) shows the better design as a optical device.

Result & Discussion

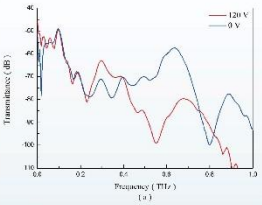

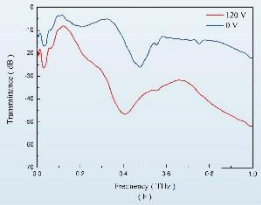

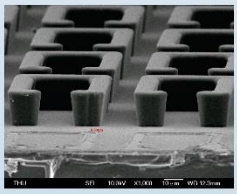

Figure (a) presents the experimental terahertz spectra of the EWOD cell with the 18 μm-thickness SRR array at applied voltages of 0 V and 120 V. At 0 V, the metamaterial that is surrounded with air exhibits a resonance peak at 0.81 THz. The peak arises from the electromagnetic resonance of the metamaterial. As a voltage of 120 V is applied to the EWOD cell, the resonance peak shifts from 0.81 THz to a lower frequency of 0.56 THz. The application of such a voltage to each adjacent pair of the electrodes drives the glycerin droplet, so the metamaterial is covered with glycerin. The metamaterial "experiences" an increase in the refractive index of a medium that surrounds it. As a result, the resonance peak of the metamaterial is redshifted at 120 V.

To compare with Fig. (a), we change the height of metamaterial pattern. Which spectrum shows in Fig. (b), and deposited 200 nm silver as metamaterial only. That sample exhibits a resonance peak at 0.48 THz and 0.41 THz when the metamaterial surrounded by air or glycerin, respectively. It presented the height of the metamaterial can enhance the tunable range of the resonance frequency.

The EWOD cell with the 18μm-thickness SRR array has a frequency tuning range with a width of 0.25 THz herein, so the cell exhibits a higher frequency tuning range than other liquid crystal cells with metamaterials. The EWOD cell with the 18μm-thickness SRR array can be used to develop passively tunable terahertz devices such as filters, absorbers, sensors, and spectral imagers.

Conclusion

In this paper, we present a new optical device in THz which is based on electrowetting-on-dielectric technology. The terahertz spectrum of the metamaterial depicts that the EWOD technology can be used to move the glycerin drop in the sample. Because the light "experiences" the change in the refractive index of the medium that surrounds the metamaterial, the sample can be used to develop passively tunable terahertz devices such as filters, absorbers, sensors, and spectral imagers.

Acknowledgments

The authors would like to thank the Ministry of Science and Technology of Taiwan for financially supporting this research under Contract No. MOST 104-2112-M-029 -004 -MY3.

Homogeneous blue phase liquid crystals by photoalignment of azo dyes

Wei-Jie Sun (孫尉傑) and Chia-Yi Huang* (黃家逸)
*chiayihuang@thu.edu.tw
[1]*Department of Applied Physics, Tunghai University, Taichung 407, Taiwan*

Abstract

Homogeneous blue phase liquid crystals (BPLCs) cells can be achieved by friction alignment . However, dust and scratches will appear in the aligning layers of the BPLC cells due to the friction alignment. Therefore, a non-contact method, photoalignment, is used to fabricate homogeneous BPLCs in this work. A BPLC cell has a configuration, glass substrate/ photoaligning layer (SD1 dyes)/ BPLC/ photoaligning layer/ glass substrate. After a linearly-polarized UV light irradiates each of the photoaligning layers, and the surface director is reoriented toward the direction perpendicular to the optical field. Experimental results show that the photoalignment can fabricate a large-area and homogeneous BPLC film.

Photoalignment

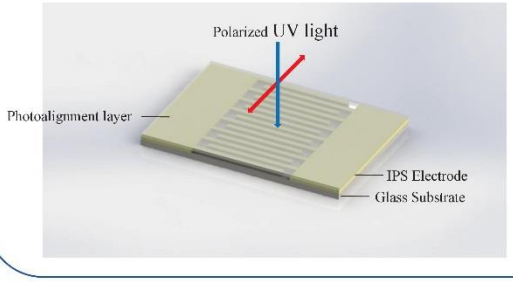

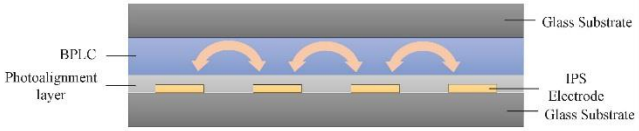

The electric field that IPS electrodes generate deforms BP lattices.

Rubbing-aligned sample

FIG. 1. Optical microscope image of anti-parallel rubbed BPLC cell.

- Monodomain BPLC
- Monochromatic color
- Scratches appear on the rubbed surfaces.

Photoalignment sample

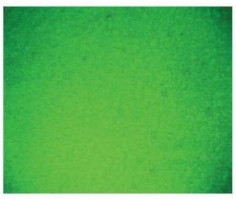

FIG. 2. Optical microscope image of photoaligned BPLC cell.

- Monodomain BPLC
- Monochromatic color
- Uniform BP lattices

Reflectance & FWHM

Rubbing-aligned alignment

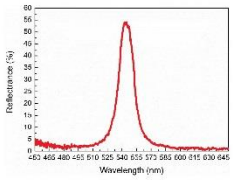

Photoalignment

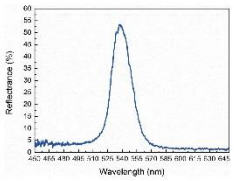

Reflectance

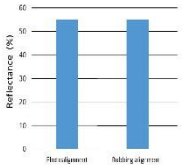

FWHM

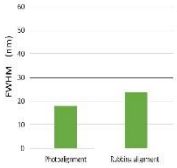

TV curve

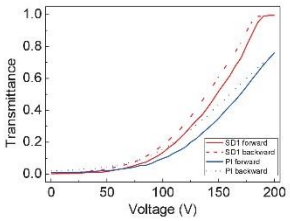

- The transmittance (0.011) of the photoaligned LC cell is half that (0.022) of the rubbed LC cell at 0 V, depicting that the former can be more regarded as an optically isotropic medium.
- Thin SD1 films have weak electric field shielding effect, so the voltage that drops on the BPLC layer is higher in the photoalignment sample than in the rubbing-aligned sample.
- The photoaligned LC cell has a smaller hysteresis than the rubbing-aligned LC cell, indicating that the uniform alignment in the photoaligned LC cell can reduce the hysteresis.

Conclusion

This work uses the SD1 dyes to photoalign the BP lattices. The photoalignment can accumulate the grow of the BP lattices, achieving the monodomain BPLC cell. Compared with the rubbing-induced BP LC cell, the photoalignment-induced BPLC cell has the advantages of no dust, defects and scratches. Application of voltages to BPLC cells also can fabricate monodomain BPLC cells [Applied Physics Letters 102, 171110 (2013)]. However, the voltage-induced BPLC cells are not permanent because there is no surface anchoring to stabilize the monodomain structure. Therefore, the photoalignment-induced BPLC cell is superior to the voltage-induced BPLC cells.

Acknowledgments
The authors would like to thank the Ministry of Science and Technology of Taiwan for financially supporting this research under Contract No. MOST 104-2112-M-029 -004 -MY3.

Homogeneous blue phase liquid crystals by photoalignment of azo dyes

Wei-Jie Sun (孫尉傑) and Chia-Yi Huang* (黃家逸)
*chiayihuang@thu.edu.tw
[1]*Department of Applied Physics, Tunghai University, Taichung 407, Taiwan*

Abstract

Homogeneous blue phase liquid crystals (BPLCs) cells can be achieved by friction alignment . However, dust and scratches will appear in the aligning layers of the BPLC cells due to the friction alignment. Therefore, a non-contact method, photoalignment, is used to fabricate homogeneous BPLCs in this work. A BPLC cell has a configuration, glass substrate/ photoaligning layer (SD1 dyes)/ BPLC/ photoaligning layer/ glass substrate. After a linearly-polarized UV light irradiates each of the photoaligning layers, and the surface director is reoriented toward the direction perpendicular to the optical field. Experimental results show that the photoalignment can fabricate a large-area and homogeneous BPLC film.

Photoalignment

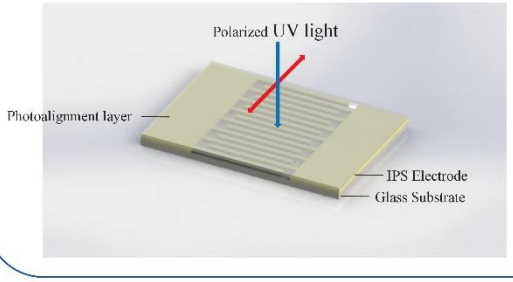

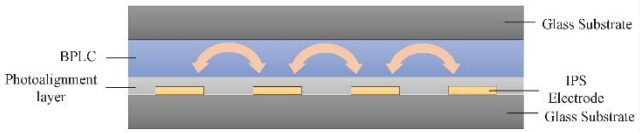

The electric field that IPS electrodes generate deforms BP lattices.

Rubbing-aligned sample

FIG. 1. Optical microscope image of anti-parallel rubbed BPLC cell.

- Monodomain BPLC
- Monochromatic color
- Scratches appear on the rubbed surfaces.

Photoalignment sample

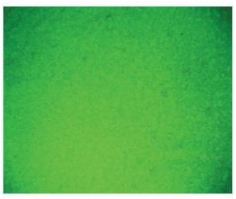

FIG. 2. Optical microscope image of photoaligned BPLC cell.

- Monodomain BPLC
- Monochromatic color
- Uniform BP lattices

Reflectance & FWHM

Rubbing-aligned alignment

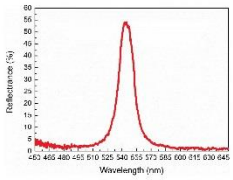

Photoalignment

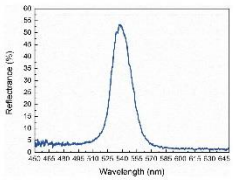

Reflectance

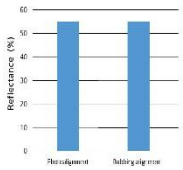

FWHM

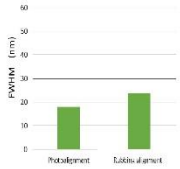

TV curve

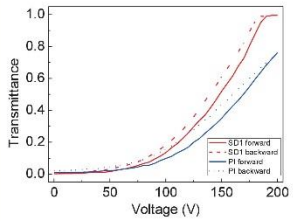

- The transmittance (0.011) of the photoaligned LC cell is half that (0.022) of the rubbed LC cell at 0 V, depicting that the former can be more regarded as an optically isotropic medium.
- Thin SD1 films have weak electric field shielding effect, so the voltage that drops on the BPLC layer is higher in the photoalignment sample than in the rubbing-aligned sample.
- The photoaligned LC cell has a smaller hysteresis than the rubbing-aligned LC cell, indicating that the uniform alignment in the photoaligned LC cell can reduce the hysteresis.

Conclusion

This work uses the SD1 dyes to photoalign the BP lattices. The photoalignment can accumulate the grow of the BP lattices, achieving the monodomain BPLC cell. Compared with the rubbing-induced BP LC cell, the photoalignment-induced BPLC cell has the advantages of no dust, defects and scratches. Application of voltages to BPLC cells also can fabricate monodomain BPLC cells [Applied Physics Letters 102, 171110 (2013)]. However, the voltage-induced BPLC cells are not permanent because there is no surface anchoring to stabilize the monodomain structure. Therefore, the photoalignment-induced BPLC cell is superior to the voltage-induced BPLC cells.

Acknowledgments
The authors would like to thank the Ministry of Science and Technology of Taiwan for financially supporting this research under Contract No. MOST 104-2112-M-029 -004 -MY3.

2016中華民國物理教育聯合會議

以火花打點器於課堂演示奈米微粒製作過程

王昌仁 郭育銘 鍾尹之 單郁翔
東海大學應用物理系

摘要

奈米材料的製作是奈米科技教育中一個重要的主題。火花放電為一種可以製作奈米微粒與碳管的奈米製程，此方法製作微粒簡單且快速，但其設備通常不易攜帶至課堂上來進行演示。在這個報告中我們使用火花打點器來進行相關演示。其器材有簡單、易取得且便宜的特性。一邊教授廷得爾效應(Tyndall effect)，一邊直接在課堂上演示奈米微粒的製作過程，學生能觀察到放電過程中奈米微粒被製造出來的現象，進而理解微粒成形的基本理論與奈米微粒可長期懸浮等概念與現象。適當的改裝後也能作為實驗課的課程，進一步討論影響放電的參數與影響微粒尺寸的工作參數。

一. 動機

奈米材料製作是奈米科技教育的重要主題之一。但通常奈米製作的實驗除要特別的設備外，其操作時間與成本花費相對較高並不易直接在課堂上演示。我們希望在教學時除了製作原理的講授之外，也能在課堂上直接的製作奈米物質可以提升同學學習興趣與印象。因此我們試圖尋找是否有更有說服力且簡單明瞭的奈米材料製作的演示實驗。在本實驗室我們已發展出用火花放電來製作奈米微粒的製程(見圖一與圖二)。其方法雖然簡單但因體積龐大而無法在課堂上直接實施因此開發此一簡易可行但原理相近的裝置來進行課堂上的即時演示。

圖一. 放電法裝置

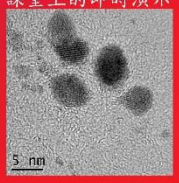

圖二. 放電法制出的金奈米微粒

二. 原理與裝置

火花放電是利用工作液介電崩潰瞬間產生出來的大電流來腐蝕樣品。其原理是當工具電擊向工件電擊靠近時，電場隨之增加，直到電場強度大於介電強度時會發生介電質崩潰，此時電弧強制解離工作液產生離子傳導，電流通過兩極，產生火花放電。在放電時會產生巨大的熱能，微量的金屬材料會被濺到工作液中冷卻，形成金屬微粒。電流停止，介電質恢復絕緣性，再重複進行上述動作。工作液是影響放電的因素之一，工作液必須是介電質，介電質是指可被極化的絕緣體。工作液必須保持低黏稠度，讓工作液流動，並回到絕緣性，再次進行放電。放電完成後要如何得知液體裡有奈米微粒呢?我們能利用廷德爾效應(Tyndall effect)來檢視。廷德爾效應是指懸浮的膠體粒子可散射經過的光線而呈現乳光現象，可以用來偵測奈米微粒的存在。

而我們在這次報告中使用的火花打點器本來是運用在運動學上，利用火花放電在紙袋上打出小孔進而得知物體的運動頻率。

為了達到可在課堂直接演示的目標有兩項裝置需克服可攜性的問題。在製作樣品的腔體方面有許多方法可以製作;圖三(a)(b)(c)為可行的示範例。(電極直接使用縫衣針即可)

圖三. (a)

圖三. (b)

圖三. (c)

另一待克服的是電源裝置;我們需要一能間歇性輸出高電壓的裝置。我們發現有兩種容易取得的裝置可使用;一為以前普物實驗室常使用的火花打點器(圖四);一為可利用市面可買到的電子點槍來加以改裝(圖五)。

圖四. 改裝傳統火花打點器作為電源;相較於電子點火槍的優點是電能較高;微粒產生較快

圖五. 改裝電子點火槍作為電源;其優點是使用電池即可運作。

三. 演示步驟與過程

我們以圖三(a)來說明演示的過程，其較特別的是一端以螺旋測微器固定於容器的一端，因此可量出放電時正負電極間的距離。

我們使用的加工液為蒸餾水(也可用逆滲透或市售包裝純水)。步驟為

1. 將針尖調製是當的距離(約 2mm)
2. 將純水加至淹沒電極
3. 以三用電表確認電極間的電阻至少大於幾十MΩ;一方面確認針尖沒有接觸,一方面確認液體為電介質而非導體態。
4. 將電源與電極連接(不須考慮正負級)
5. 準備一隻雷射筆使雷射光經過水中觀察是否有乳光產生，若容器與水是乾淨的應不會發現乳光(圖六)。
6. 啟動電源，此時電極間應會間歇出現火花
7. 約幾分鐘後將發現乳光逐漸出現並越來越清楚(圖七)。

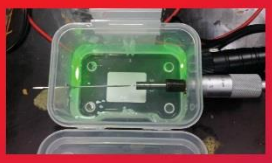

圖六. 放電開始前未觀察到乳光出現

圖七. 放電約三分鐘後已有明顯乳光訊號

四. 討論與結語

利用火花放電加工的原理以火花打點器(或電子點火槍)做為電源可以成功地在課堂上即時製作出奈米金屬微粒。其優點為:

1. 所需花費不高;
2. 可即時製作微粒加深學生印象;
3. 可結合乳光現象與學生探索奈米微粒的製作過程與物理特性。

可適用於各級學校來教授。

另外此裝置若經適當地擴充也可發展成為一個大學的實驗課程，讓學生進一步探討不同介電質、不同電級距離、不同電級材質與工作電壓等對於奈米微粒製作的影響。

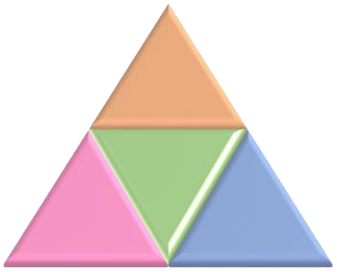

東海大學應用物理系